Diffraction Correction in Ultrasonic Fields for Measurements of Sound Velocity in Gas. Conventional and Alternative Methods.

Espen Storheim[a,c,*], Per Lunde[a,b,c], and Magne Vestrheim[a,c]

[a] *University of Bergen, Department of Physics and Technology, Postboks 7803, N-5020 BERGEN, Norway*
[b] *Christian Michelsen Research AS (CMR), P.O. Box 6031 Postterminalen, N-5892 BERGEN, Norway*
[c] *The Michelsen Centre for Industrial Measurement Science and Technology*

Abstract

Correction for ultrasonic transducer diffraction effects is discussed and evaluated in relation to realizing a precision sound velocity cell within $100 - 200$ ppm relative uncertainty (95 % conf. level), for use in custody transfer energy measurement of natural gas at elevated pressures. In this application, and at laboratory conditions, the diffraction correction phase might preferably be known within $0.5°$, tentatively, in the $150 - 200$ kHz operational frequency range of ultrasonic multipath fiscal flow meters. For actual transducers in such applications, traditional diffraction correction models based on the "piston model" are found to be not sufficiently accurate over the frequency band of interest. A simplified finite element based diffraction correction model (SFDC) is used to investigate and evaluate the diffraction correction for more realistic transducer vibrations, such as for unbaffled and baffled circular piezoceramic disk elements vibrating at, below and around their important first and second radial mode, R1 and R2, respectively. The contributions to the magnitude and phase of the diffraction correction frequency response are discussed, in relation to the traditional diffraction correction models, over the frequency band of interest.

1. Introduction

In earlier work (e.g. [1–4]) piezoelectric transducers have been used to evaluate candidate methods for a precision sound velocity cell for natural gas at elevated pressures. In this work, transducer diffraction effects and accurate correction for such effects, appear to be among the most critical factors in order to realize a high precision measurement cell [2–4].

It is well known that accurate correction for transducer diffraction effects is necessary for precise sound velocity measurements. Early measurements of sound velocity and attenuation in various media indicated an effect which was dependent on the distance between the transmitter and receiver [5–9]. A change of the signal amplitude and a time shift of the signal different from that of a plane wave were experienced, for all other parts of the signal than the signal onset. A model was proposed by Williams [10] to describe these effects of transducer diffraction, based on the model for a plane circular piston mounted in a rigid baffle of infinite extent, vibrating with uniform velocity amplitude and phase (here referred to as the "baffled piston model").

Williams' diffraction theory for the "baffled piston" was later used by Khimunin [11–13] and others [14–20] to formulate a "diffraction correction" relative to plane waves. In Khimunin's [11, 12] approach, the diffraction correction is defined as the ratio of the free-field average sound pressure in the propagation medium (integrated over a circular "measurement area" corresponding to the receiving transducer front, in absence of the receiving transducer) - to - the plane-wave sound pressure in the fluid at the centre point of the receiving transducer front (in absence of the receiving transducer). Cf. Eq. (1) below.

Figure 1 shows a calculation [21–23] of the time shift of a real wave signal in the far field of a transmitting transducer relative to the corresponding plane wave signal, for the transient starts of the two signals, employing Khimunin's model for the diffraction correction. While the signal onset is the same for both signals, the time delay between corresponding zero crossings of the two signals increases for later periods, to reach a limiting value of $-90°$ for the stationary parts of the "real" signal relative to the plane wave signal. In the

*Corresponding author
Email address: `Espen.Storheim@ift.uib.no` (Espen Storheim)

near-field the results will be different but similar.

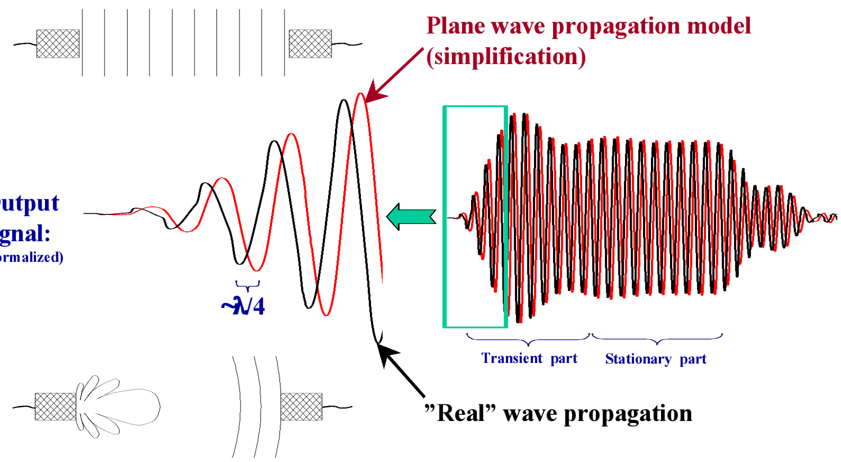

Figure 1: Schematic illustration of the simulated [21–23] effects of transducer diffraction on the time shift of an ultrasonic signal (in the far field) relative to the corresponding plane wave propagation model (after [23]).

The literature on diffraction correction following these early investigators is considerable, due to its importance in the analysis of a variety of acoustic systems. Traditionally, for more than fifty ears, the baffled piston model has been widely used to evaluate transducer diffraction effects.

Classical examples where transducer diffraction effects need to be addressed and corrected for, are e.g. precise measurements of the attenuation of sound velocity in fluids and solids, involving the magnitude and phase of the diffraction correction, respectively. Other examples include transducer calibrations, ultrasonic custody transfer metering of gas (volumetric, mass and energy flow metering), and sound velocity cells for gas characterization [1–4].

In these methods, transducer diffraction effects have been corrected for in a simplified manner. At the transducer vibration modes employed, the radiating and receiving transducers do not necessarily vibrate uniformly as plane pistons, and radiation and reception of sound will also occur at the sides and rear of the transducer, possibly causing interference with the waves propagating directly between the front faces of the transducers.

These issues raise questions of (1) how accurate is the traditionally applied plane piston diffraction correction model for the different vibration modes of the transducer, and (2) can this plane piston diffraction correction model be used for real transducers used e.g. in the sound velocity measurement cell investigated in [1–4]?

As an improved but still simplified approach to account for such effects (for the transmitting transducer only), a method was proposed in [22, 23] for description of the diffraction correction of an acoustic receiver located in the sound field of a non-uniformly vibrating and finite-sized transmitting transducer. This method extends the more traditional models for diffraction correction by accounting for (a) arbitrary non-uniform vibration of the transmitting transducer (e.g. different vibration modes), and (b) radiation from all parts of the transmitter (the front, side and rear surfaces). For diffraction at the receiver, the received signal was taken as the average freefield pressure over the receiver front surface, as in the simplified Williams-Khimunin approach. This model (here referred to as the "simplified finite element diffraction correction method" (SFDC)) was used to illustrate the importance of such extensions. Finite element modelling (FEM) was used to calculate the piezoelectric transducer vibrations, the resulting sound field, and the diffraction correction, for an example of an unbaffled piezoelectric transducer operating in gas, for the relevant frequency band of the transducer (involving different transducer vibration modes, such as the important radial modes). The magnitude and phase of the diffraction correction for the transducer were compared with the classical "baffled piston model" approach. Significant deviations from the uniform piston diffraction correction were demonstrated for various vibration modes of the transducer, both for the magnitude and the phase. Such deviations were ascribed qualitatively to non-uniform transducer vibration and radiation from the sides and rear surfaces of the transmitting transducer, but the details of the complex mechanisms involved have not been fully understood.

In the present work, as an attempt to improve the understanding of the properties of the diffraction correction for real piezoelectric transducers and their vibration modes, the complex mechanisms involved are analyzed by considering a simplified transducer construction, a single circular piezoceramic disk element vibrating in air. The diffraction correction is studied using the SFDC method for the lower part of the frequency spectrum, covering the important fundamental radial mode (R1) and the first radial mode overtone (R2) of the vibrating element. To gradually introduce the full complexity of effects, the baffled uniform piston diffraction correction is compared with the diffraction correction of a baffled piezoceramic disk, and with the corresponding unbaffled piezoceramic disk. This approach is of scientific interest, as it represents the next step in complexity relative to the conventional and considerably simplified uniform piston diffraction correction model, towards understanding the diffraction correction of a full transducer construction, such as e.g. the one investigated in [22, 23] (a circular piezoceramic disk element with matching and backing layers).

Using this approach, the two questions (1) and (2) above are investigated in relation to the candidate measurement methods for the precision sound velocity cell for natural gas at elevated pressures [1–4]. Tentative requirements for the diffraction correction for the two candidate methods are discussed and indicated.

As pointed out above, while the SFDC method includes a full FEM description of the transmitting transducer, it does not account for the full diffraction effects at the receiving transducer, such as reception at the sides and rear of the transducer. In spite of that, the SFDC method is considered to represent a step forward towards a full description of diffraction effects in a transmitter-receiver measurement system. Work is in progress experimentally and theoretically to include a full description of the receiver, to obtain a more complete description and treatment of the diffraction effects. The relatively simple case of a piezoceramic disk element as well as more complex transducer constructions are addressed in this context.

2. Theory

2.1. Introduction

The traditional description of the diffraction correction dates back to Williams [10], with a plane, circular, and uniformly vibrating piston source mounted in a rigid baffle of infinite extent, and a circular "measurement area" in the fluid, normal to the source axis, at the position of the receicer. In Williams' description, the diameter of this "measurement area" was equal to the diameter of the transmitter. This is illustrated in Figure 2 when $b = a$, where a is the radius of the transmitter and b is the radius of the receiver. The so called "measurement area" is rather an observation area, since there is no physical receiver present in the acoustical pressure field.

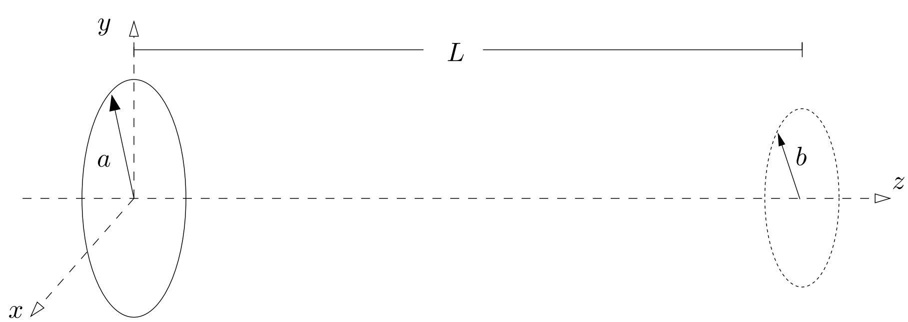

Figure 2: Illustration of a plane piston source (left) and a "measurement area" (right), with parallel faces and aligned on-axis. The transmitter is placed in the $xy-$plane at $z = 0$, and the "measurement area" at $z = L$.

The diffraction correction as defined by Khimunin [11] as[1]

$$H^{diff} = \frac{\langle p \rangle}{p^{plane}}, \tag{1}$$

[1] Here, a slightly different notation than in [11, 12] is used.

where $\langle p \rangle$ is the average pressure over the "measurement area" at distance $z = L$ (in absence of the receiver), and p^{plane} is the plane wave pressure at the same distance. This correction is a complex quantity where the magnitude and phase are used to correct the deviation in amplitude and the phase lag from plane waves, respectively. The phase correction corresponds to a *diffraction time shift*, given as $t^{diff} = -\angle H^{diff}/\omega$, where $\omega = 2\pi f$ is the angular frequency, and f is the frequency. Even though it is a simplification of actual conditions, the results found in [11, 12] are still in use today, and do provide a good indication of the influence of diffraction effects. However, in some cases where high-precision diffraction correction is required, more detailed methods are needed [22, 23].

In the present paper, the various expressions for the diffraction correction are written with the dimensionless quantities S and ka. $S = z\lambda/a^2$, where z is the axial distance $\lambda = 2\pi/k = c/f$ is the wavelength, $k = \omega/c$ is the wave number, c is the speed of sound, and a is the radius of the transmitter.

2.2. Khimunin's model

Based on Williams' theory for a baffled plane piston [10], Khimunin formulated and calculated the diffraction correction for the magnitude [11] and phase [12]. His results are valid for a uniformly vibrating piston with radius a and an equal "measurement area" at distance $z = L$, i.e. $b = a$ in Figure 2, giving

$$H^{diff}(ka, S) = 1 - \frac{4}{\pi}\int_0^{\pi/2} \exp\left[-i\frac{(ka)^2 S}{2\pi}\sqrt{1 + \left(\frac{4\pi}{Ska}\right)^2 \cos^2(\theta)}\right] \sin^2(\theta)\,\mathrm{d}\theta, \tag{2}$$

where θ is an integration variable. There are no analytical solutions for the general case, i.e. arbitrary ka, so numerical methods must be used.

2.3. Beissner's model

Khimunin's approach has some limitations. For instance, the transmitter is a plane piston, and the "receiver" is of equal size as the transmitter. This is generally not the case in real measurement scenarios, when measuring with e.g. microphones or hydrophones. This problem has been addressed by Yamada and Fujii [16], and Beissner [20], where the diffraction correction is solved for an arbitrary receiver size. The ratio $\gamma = b/a$, which is the ratio of the radius of the receiver to that of the transmitter, is used. The expression for $\gamma \leq 1$, i.e. for a "measurement area" equal to or smaller than the transmitter, can be written in terms of S and ka as

$$H^{diff}(ka, S, \gamma) = 1 - \frac{2}{\pi\gamma^2}\int_{1-\gamma}^{1+\gamma} \sqrt{1 - \left(\frac{1-\gamma^2+\xi^2}{2\xi}\right)^2} \times \exp\left[-ika(\sqrt{\xi^2 + (\eta S)^2}) - \eta S\right]\mathrm{d}\xi, \tag{3}$$

where $\eta = ka/2\pi = a/\lambda$, and ξ is an integration variable. This integral must also be solved numerically since no analytical solution exists. The expression for $\gamma \geq 1$ is very similar [20] but is not discussed in the present study.

2.4. On-axis point receiver (piston model)

The on-axis pressure from an uniformly vibrating plane piston, placed in a rigid baffle of infinite extent, is given as [24]

$$p(z, t) = \rho c v e^{i(\omega t - kz)}\left[1 - \exp\left\{-ik\left(\sqrt{z^2 + a^2} - z\right)\right\}\right], \tag{4}$$

where ρ is the density of the medium, and v is the particle velocity of the piston source. The diffraction correction for a point receiver is found from Eq. (4) by dividing by the plane wave pressure, $p^{plane} = \rho c v e^{i(\omega t - kz)}$. With the introduction of S and ka, the expression can be written as

$$H^{diff}(ka, S) = 2\sin\left[\frac{(ka)^2 S}{4\pi}\left(\sqrt{1 + \left(\frac{4\pi}{Ska}\right)^2} - 1\right)\right] \times \exp\left[i\left(\frac{\pi}{2} - \frac{(ka)^2 S}{4\pi}\left(\sqrt{1 + \left(\frac{4\pi}{Ska}\right)^2} - 1\right)\right)\right], \tag{5}$$

which is an exact solution, expressed in terms of its magnitude and phase. This expression presents an approximation for $a \gg b$, such as for measurements with e.g. a needle hydrophone.

2.5. Comparison of the traditional methods

One of the benefits of Beissner's model is that the size of the receiver can be varied over a large range, $0 \leq b \leq a$ and $b > a$. To illustrate this, the size of the receiver is varied from $b = a$ to $b \to 0$, and compared with Khimunin's model and the on-axis point receiver. This is shown i Figure 3 for both the magnitude and phase, where they are plotted as a function of the dimensionless distance S, for $0 \leq S \leq 10$.

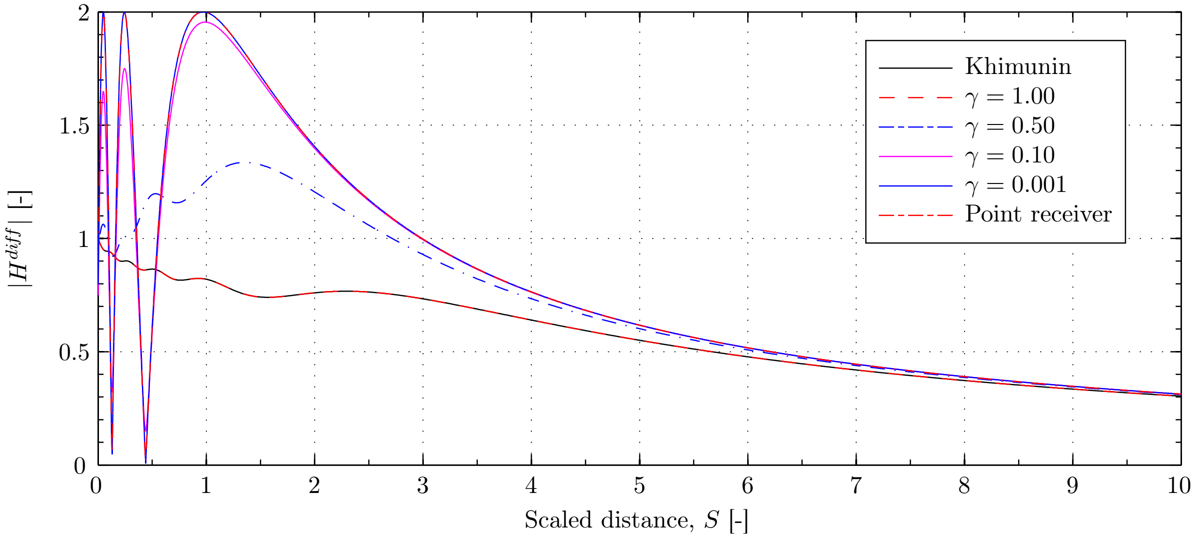

(a)

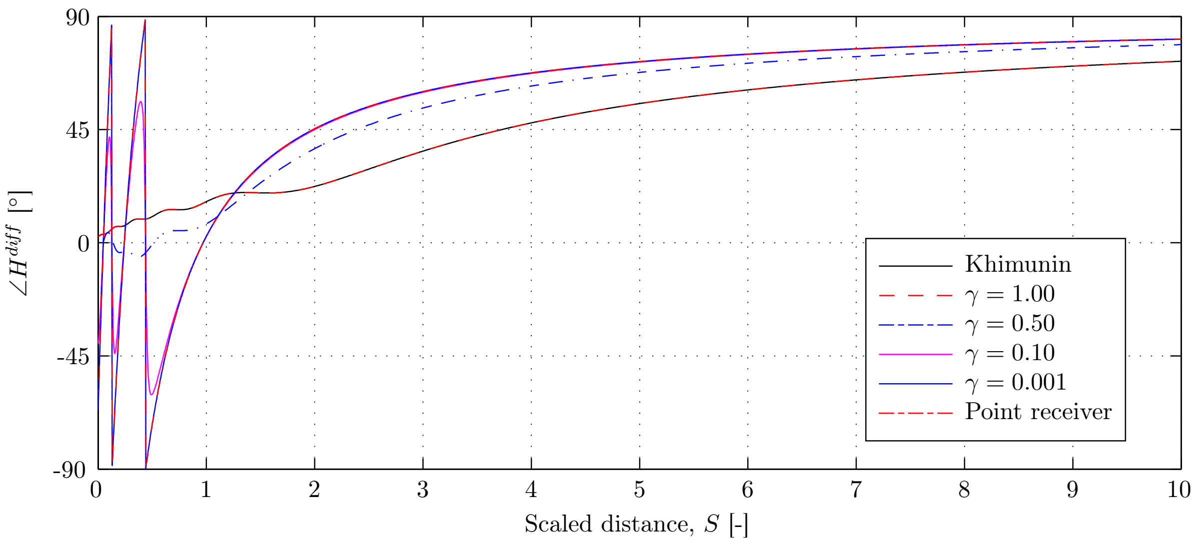

(b)

Figure 3: Comparison between Khimunin's model, Beissner's model, and the on-axis point receiver model, for the diffraction correction, where $0 \leq S \leq 10$. Different values of γ are presented to illustrate the agreement of Beissner's model with Khimunin's model and the point receiver model, as $\gamma \to 1$ and $\gamma \to 0$, respectively, for $ka \approx 18$. (a) Magnitude. (b) Phase.

Although it is difficult to see in Figure 3, Beissner's model does converge to the on-axis point receiver as $\gamma \to 0$. Similarly, the model converges to Khimunin's model as $\gamma \to 1$. The limits as $S \to \infty$ are 0 and 90°, for the magnitude and phase respectively. For $S = 10$, neither the magnitude nor the phase have converged to these limits. Figure 3a shows that the diffraction correction for various receiver sizes converge towards the same $1/S$ dependency.

2.6. Simplified Finite-Element Diffraction Correction method

The *Simplified Finite-Element Diffraction Correction method* (SFDC) [22, 23] represents an alternative and more powerful method to calculate the diffraction correction. The definition of the diffraction correction is the same as in [11], i.e. Eq. (1), but the full transmitting piezoelectric transducer is taken into account, not just a plane piston. This includes radiation from all parts of the body, internal waves in the transducer and non-uniform vibration of the transmitting transducer. This is a more appropriate description of real conditions than for the traditional methods. However, the receiver is still represented by a "measurement area" such as for the traditional methods, as indicated in Figure 4.

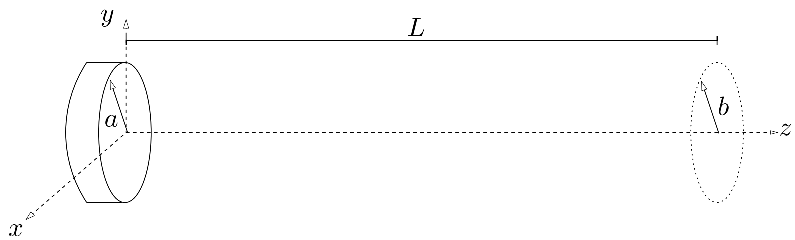

Figure 4: Illustration of the configuration used here for the SFDC, where a circular piezoceramic disk is used as an example of a transmitter. Note that this method is not restricted to $b = a$, nor to this specific type of transmitter, as a full transducer construction could be used. Also, the transmitter could be baffled or unbaffled, cf. Figure 6. The front of the transmitter is placed at $z = 0$, and the "measurement area" at $z = L$.

The theory behind this method is described in [22, 23][2], but the main principles are repeated here. The first step is to calculate the pressure $\langle p \rangle$ radiated by the piezoelectric transmitting transducer in the fluid, averaged over the "measurement area" at distance $z = L$. Then, the far-field on-axis pressure p_{ff} at a very long distance z_{ff} (e.g. 1000 m), for a lossless medium, is calculated. This pressure is extrapolated back to the source using the baffled piston model, in order to calculate the particle velocity of an equivalent piston, i.e. the required velocity of a piston of equal radius as the transmitting transducer in order to generate that particular farfield pressure p_{ff}. This is called the "equivalent piston velocity", and is given as

$$v_0^{eq,pist} = p_{ff} \frac{2z_{ff}}{i\rho cka_{eq}^2} e^{ikz_{ff}} = p_{ff} \frac{z_{ff}}{i\rho f A_{eq}} e^{ikz_{ff}}, \tag{6}$$

where the time-harmonic dependency $e^{i\omega t}$ is neglected, and $A_{eq} = \pi a_{eq}^2$ is the area of the equivalent plane piston. The velocity of this piston is in turn used to calculate the equivalent plane wave pressure at the distance $z = L$, $p^{eq,plane}$, i.e.

$$p^{eq,plane} = \rho c v_0^{eq,pist} e^{-ikz} = p_{ff} \frac{2z_{ff}}{ika_{eq}^2} e^{ik(z_{ff}-z)}. \tag{7}$$

Both pressures in Eq. (1), $\langle p \rangle$ and $p^{eq,plane}$, are in the present paper calculated using the finite element method[3]. The diffraction correction is then given according to Eq. (1) as [22]

$$H^{diff} = \frac{\langle p \rangle}{p^{eq,plane}} = \frac{\langle p \rangle}{2z_{ff} p_{ff}} ika^2 e^{-ik(z_{ff}-z)}, \tag{8}$$

where $a_{eq} = a$ is the radius of the transmitting transducer.

An important feature of the SFDC is that the sound field is calculated using a full description of the piezoelectric transducer, included the transducer's transmitting properties. However, in the calculation of H^{diff} using the SFDC, the transducer properties vanishes [22, 23], so that only diffraction properties in the radiated field are accounted for.

[2]Eq. (2) in [23] contains a mistype. It should read $u_0^{eq,pist.} = p_{ff} z_{ff} e^{ikz_{ff}} / i\rho f$. However, the results in [23] are not affected by this.

[3]The finite element software used in the present study is FEMP 5.0 [25–28].

2.7. Sound velocity cell and uncertainty in diffraction correction

For use in connection with custody transfer energy measurement of natural gas using multipath transit time ultrasonic flow meters (USMs) [1, 3, 29–31], the expanded measurement uncertainty of the sound velocity cell investigated in [1–4] should preferably be less than $(0.05 - 0.1)$ m/s (95 % conf. level), in natural gas at operating pressures and temperatures ($0 - 60°$ and $5 - 250$ bara, tentatively) [1]. This corresponds to a relative expanded uncertainty of $100 - 200$ ppm (parts per million) (95 % conf. level). The measurement uncertainty of the cell should be traceable to national and international standards. To avoid or reduce measurement errors due to possible dispersion in the gas, the VOS cell should operate in the operational frequency range of USMs, $100 - 200$ kHz [1].

At significantly more controlled conditions in the laboratory, using e.g. air, nitrogen or argon at room temperature and atmospheric conditions, the expanded measurement uncertainty of the sound velocity cell should preferably be less than $0.01 - 0.02$ m/s (95 % conf. level), corresponding to a relative expanded uncertainty of $20 - 40$ ppm (95 % conf. level),

The measurement cell investigated in [1–4] (cf. Section 1) is designed to operate with two different methods in measurement of the speed of sound in gas. The reasoning for the choice of these specific measurement methods is extensive [1], but there is one benefit worth mentioning here. A traditional method to determine the speed of sound in a medium, is to measure the time it takes for a pulse to propagate a certain distance. However, a certain time delay is present in the transmitting and receiving electronics and transducers, resulting in a higher measured transit time than the propagation time in the medium. Consequently, a lower speed of sound is calculated. When high accuracy is required, these effects must be compensated for. Determining these delays may prove difficult, so another approach is to use alternative techniques where the delays are reduced or cancelled by the measurements. Two examples of such methods are the three-way pulse method (3PM) [1, 4] and the two-way pulse echo method (2PEM) [4, 32], illustrated in Figure 5. These are the methods which were used in the measurement cell [4].

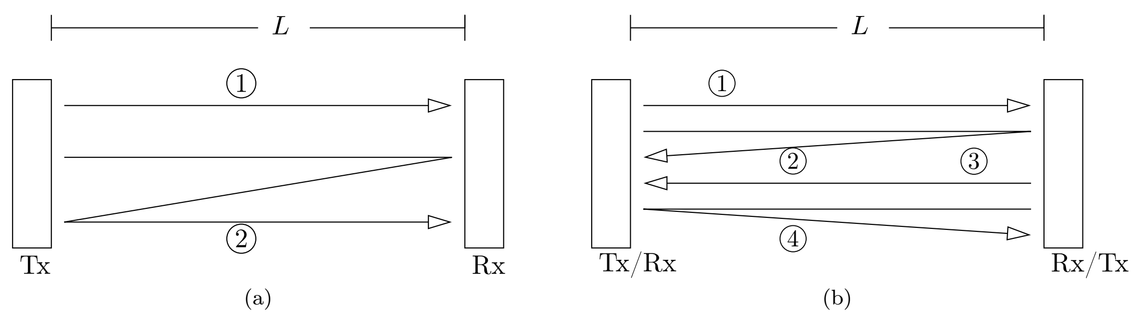

Figure 5: Principle sketches of the two candidate sound velocity measurement methods under investigation. The numbers indicate the numbering of the acoustic signals. (a) Three way pulse echo method, 3PM [1, 4]. (b) Two way pulse echo method, 2PEM [4, 32].

For the 3PM (Figure 5a), one transducer is the transmitter and the other the receiver. The direct signal and the twice reflected signal are recorded, with a total travelling distance of L and $3L$ respectively. For the 2PEM (Figure 5b), the direct signal and the once reflected signal are recorded, where the transmitter acts as a receiver in the latter case. Then, the same procedure is repeated with the transducers in opposite roles. The maximum travelling distance for the pulse is $2L$, hence a higher signal to noise ratio is expected compared to the 3PM, if the conditions are equal. Also, signals 2 and 4 in the 2PEM are only reflected one time, compared with two reflections for signal 2 in the 3PM. However, due to the fact that the transducers must switch between acting as a transmitter and a receiver, an electronic switching circuit is required. Such a circuit may introduce noise and other unwanted effects [4].

For both these measurement methods, the speed of sound is given as [1, 4, 32]

$$c = \frac{2K_T L_0}{\Delta t - t^c}, \tag{9}$$

where K_T is a correction for the thermal expansion in L_0, L_0 is the distance measured at a reference temperature T_0, Δt is a difference between recorded transit times, and t^c is a time correction term. The expressions for Δt and t^c for the two models are [1, 4]

$$\text{3PM:} \qquad \Delta t = t_2 - t_1, \qquad t^c = t_2^c - t_1^c \approx 2(t^{diff,r} + t^{tv}).$$

$$\text{2PEM:} \qquad \Delta t = t_2 - t_1 + t_4 - t_3, \qquad t^c = t_2^c - t_1^c + t_4^c - t_3^c \approx 2(t^{diff,r} + t^{tv}),$$

where the various subscripted numbers correspond to the signals in Figure 5. The correction terms t^c account solely for acoustic time delay effects due to diffraction time correction (t^{diff}), thermal and viscous boundary layers at a reflecting surface (t^{tv}), and internal transducer reflections (t^{int}) [1] (which are assumed to be negligible [4]). In the above approximation, the direct signal (1 in 3PM, and 1 and 3 in 2PEM) is said to be equal to the direct signal in the pulses which are reflected, i.e. 2 in 3PM and 2 and 4 in 2PEM. Thus, the remaining parts are the reflected signals, and the difference in propagation length used in Δt is $2L$ for both methods. Consequently, the correction terms are said to consist of the diffraction correction for the reflected signals ($t^{diff,r}$), which have been assumed equal for every reflection [4], and the thermal and viscous effects upon reflection (t^{tv}) [1, 4].

The relative expanded uncertainty of the speed of sound is given as [1, 4, 33]

$$\frac{U(c)}{c} \approx k\sqrt{\left(\frac{u_c(K_T)}{K_T}\right)^2 + \left(\frac{u_c(L_0)}{L_0}\right)^2 + \left(\frac{u_c(\Delta t)}{\Delta t}\right)^2 + \left(\frac{u_c(t^c)}{\Delta t}\right)^2}, \tag{10}$$

where $U(c)$ is the expanded uncertainty of c, k is the coverage factor[4] [33] and it has been assumed that $\Delta t \gg t^c$. A 95 % confidence interval, i.e. $k = 2$, is used. $u_c(\,\cdot\,)$ is the combined standard uncertainty of the argument [33].

A simple calculation is performed to illustrate the importance of the uncertainty in t^c. Assume the same conditions for the two measurement methods, a separation distance of $L = 15$ cm in air with $c = 343\,\mathrm{m\cdot s^{-1}}$ and no dispersion. Consider a tentative requirement that $u_c(t^c)/\Delta t \leq 20$ ppm, which corresponds to $u(t^c) \leq 8.75$ ns. The corresponding uncertainty in $\angle H^{diff}$ is then given as

$$u(\angle H^{diff}) \leq \omega u(t^c), \tag{11}$$

where the uncertainty in the phase of the diffraction correction increases linearly with the frequency. For $f = 150$ kHz the tentative requirement $u_c(t^c)/\Delta t \leq 20$ ppm corresponds to $u(\angle H^{diff}) \leq 0.5°$. This tentative uncertainty is comprised of all the contributions to the diffraction, including those which corresponds to reflection at a transducer.

3. Results

3.1. Transducer properties and simulation parameters

The simulations are performed with the finite element program FEMP 5.0 [25–28]. A single Pz27 piezoceramic disk with diameter $D = 12.7$ mm and thickness $T = 2$ mm, i.e. a D/T ratio of 6.35, is studied. The "measurement area" is placed at $L = 15$ cm, as used in the measurement cell described in [4]. Note that the present simulations only account for the direct signal, so that reflection from the receiver are not considered, cf. Figure 4. At 155.5 kHz in air (at the R1 mode) the Rayleigh distance, given by $Z_R = \pi a^2/\lambda$, is approximately 5.7 cm, and 14.1 cm at 400 kHz, which is the upper frequency in the simulations in the present study. The surrounding medium is air with $c = 343\,\mathrm{m\cdot s^{-1}}$ and $\rho = 1.205\,\mathrm{kg\cdot m^{-3}}$. More details on the simulations are given in Appendix A.

Two different setups for the piezoceramic element are compared in the following: The element without a baffle and the placed in a rigid baffle of infinite extent.

[4]Not to be confused with the acoustic wave number $k = \omega/c$.

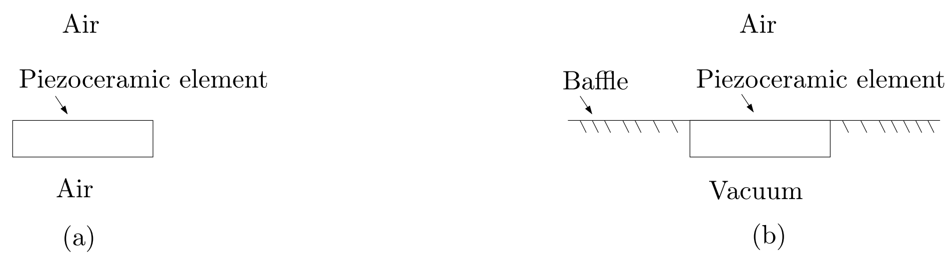

Figure 6: The two radiation cases studied: (a) A circular piezoceramic element vibrating in air without a baffle. (b) A circular piezoceramic element mounted in a rigid baffle of infinite extent, vibrating in air at the front half space, and into vacuum at the sides and the rear surface.

When the piezoceramic disk is mounted in a rigid baffle of infinite extent (here referred to as "baffled"), vacuum is placed on the sides and on the rear surface of the element, and the front surface radiates in air. The baffle is mounted flush with the front surface of the element, as seen in Figure 6b. When the element is not placed in the baffle (referred to as "unbaffled"), the entire element radiates in air, as seen in Figure 6a. Figure 8 shows the simulated source sensitivity magnitude, $|S_V|$, for the piezoceramic element in air, unbaffled and baffled. In the sensitivity plot, ripples, hereafter referred to as "undulations", are observed for frequencies below 100 kHz for the unbaffled case, including a "dip" at 9 kHz. These are not observed in the baffled case, nor in the electrical conductance, indicating that radiation from the sides and possibly the rear face of the element, interfering with the front face radiation, may be the source of these effects. A comparison of simulated and measured electrical conductance and source sensitivity, is also shown for the present element in [34], along with the material data for the piezoceramic element and air, which are used in the FEM simulations.

In the following figures, the phase shown is the "slow phase", i.e. the complex pressure divided by the plane wave term e^{-ikz}, at $z = L = 15$ cm. The slow phase is thus the deviation in phase of the actual wave, from that of a plane wave.

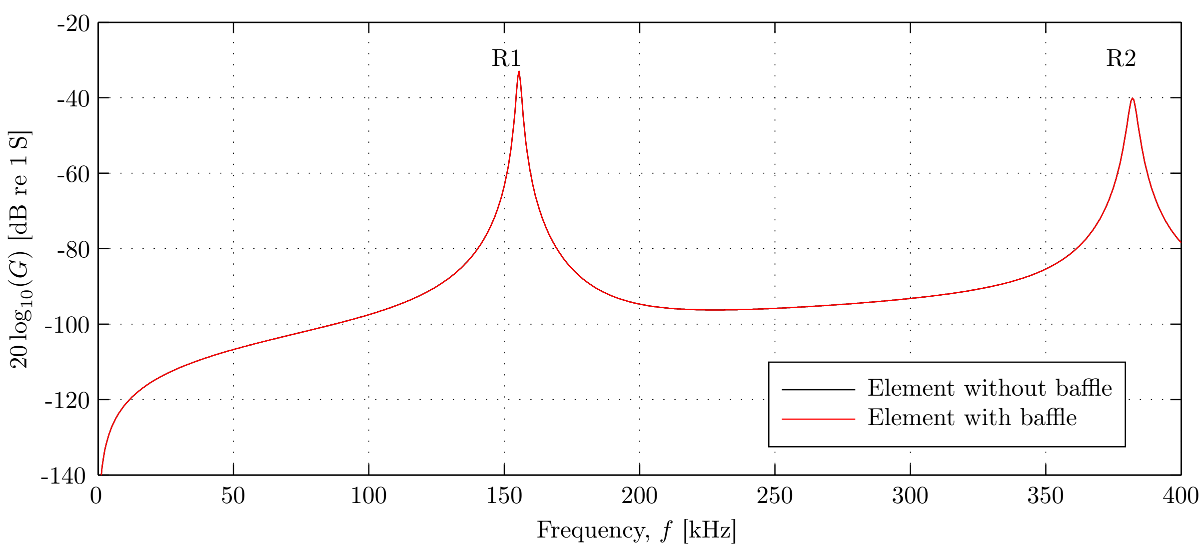

Figure 7: FEM simulation of the electrical conductance G for the Pz27 piezoceramic element, unbaffled and baffled, vibrating in air.

Figure 7 shows the simulated electrical conductance of the piezoceramic element, unbaffled and baffled. The electrical conductance reveals that the first and second radial modes (R1 and R2) of the piezoceramic element, i.e. the two series resonance peaks, are located at 155.5 kHz and 382 kHz, respectively. The conductance is practically equal for both cases, as expected.

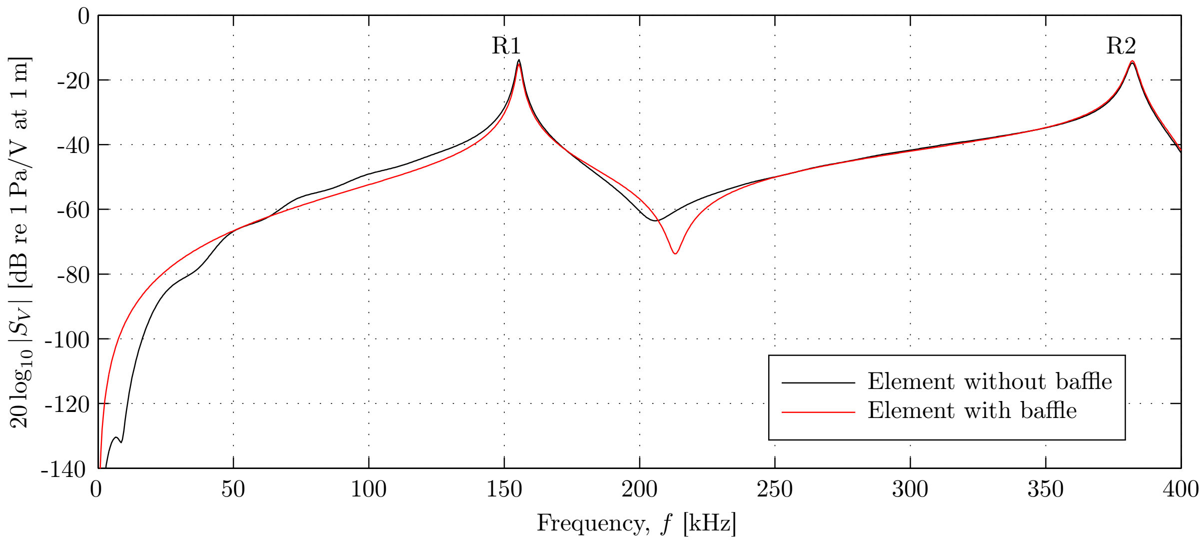

Figure 8: FEM simulation of the source sensitivity S_V for the Pz27 piezoceramic element, unbaffled and baffled, vibrating in air. The magnitude is shown.

3.2. Diffraction correction as a function of frequency

In the following section, the magnitude and phase of the diffraction correction H^{dif} are calculated with Khimunin's model and the SFDC, and compared. Two different cases are presented. One where the piezoceramic element is mounted in a rigid baffle of infinite extent, and one where the piezoceramic element is unbaffled. For each case, the magnitude and phase of the diffraction correction calculated with the two methods are shown (Figure 9 and 11). In addition, the magnitude and phase of H^{diff} are shown together with the magnitude and phase of the average pressure $\langle p \rangle$ and the equivalent plane wave pressure $p^{eq,plane}$ (Figure 10 and 12). Lastly, the magnitude and phase of H^{diff} for the two cases, i.e. unbaffled and baffled element, are shown together in Figure 13..

Figure 9 shows the diffraction correction H^{diff} for the baffled piezoceramic element, with a "measurement area" with the same diameter as the transmitter, and placed at a constant separation distance of $L = 15$ cm. The frequencies range from 0 Hz to 400 kHz, covering the first and second radial mode of the piezoceramic element. The magnitude, shown here in dB relative to 1 Pa/Pa, and the phase, given in degrees, are calculated for Khimunin's model and the SFDC.

For the magnitude shown in Figure 9a, good agreement between the SFDC and Khimunin's model is observed, over large portions of the frequency range which is investigated. However, there is a significant deviation around the peak in the SFDC at 214 kHz, which extends from approximately 175 kHz to 230 kHz. At 230 kHz, the SFDC intersects with Khimunin's model, and the magnitude is slightly lower than for Khimunin's model until they intersect again at 395 kHz. The magnitude of the peak at 214 kHz is 10 dB, and the deviation from Khimunin's model is approximately 17 dB. Since the magnitude of the peak is positive, the average pressure $\langle p \rangle$ is greater than the equivalent plane-wave pressure $p^{eq,plane}$. The location of this peak is the same as the "dip" in the source sensitivity plot shown in Figure 8, at 214 kHz. As the frequency approaches 400 kHz, an increase in the magnitude of the SFDC results is observed. The slope of this increase is similar to the one at the peak at 214 kHz. This indicates that a similar peak is present in the SFDC results, corresponding to another "dip" in the source sensitivity, above 400 kHz.

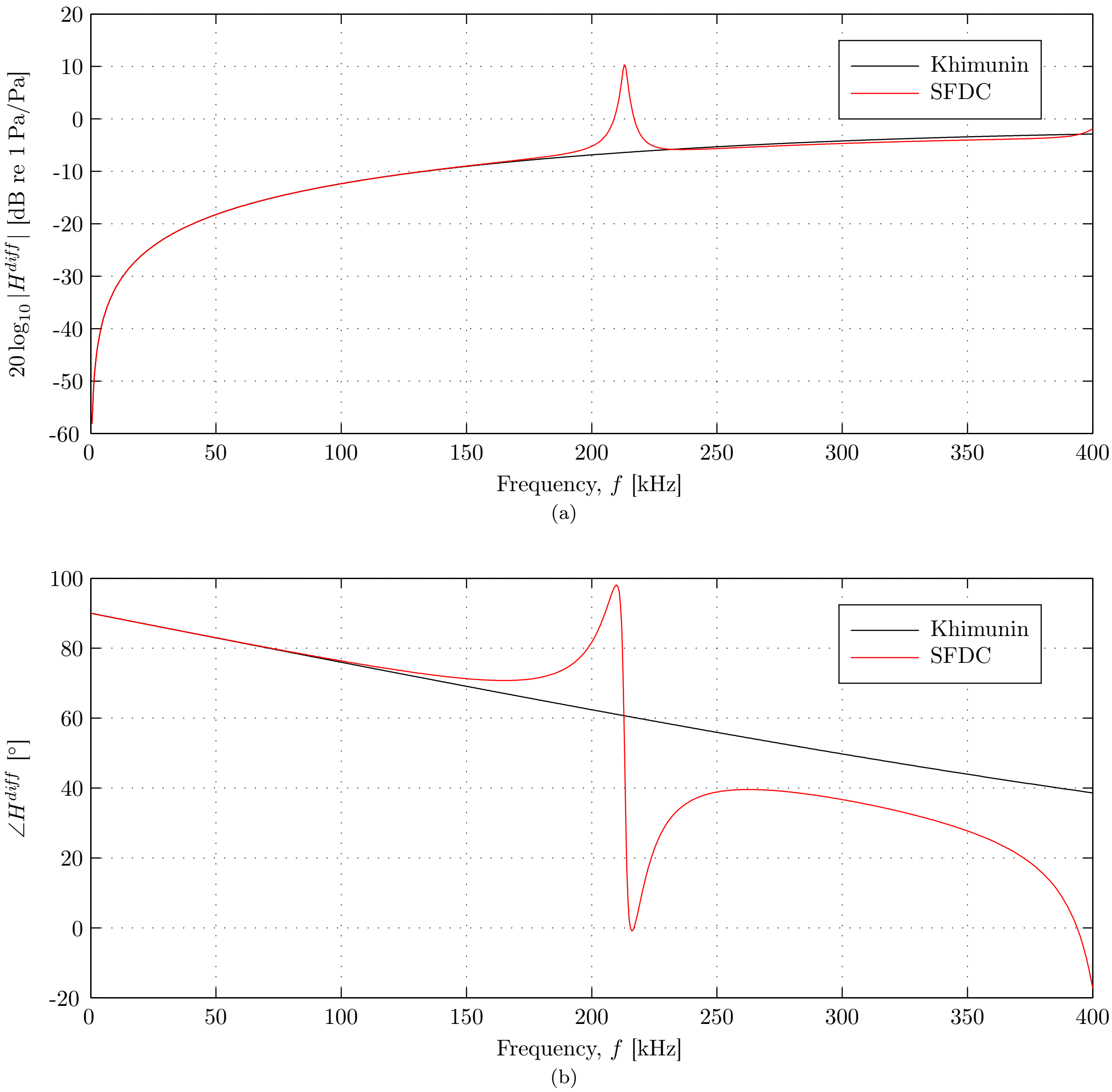

Figure 9: Comparison of the diffraction correction H^{diff} as a function of frequency, calculated using Khimunin's model and the SFDC, for the Pz27 piezoceramic element ($D = 12.7$ mm, $T = 2$ mm) vibrating and radiating in air, mounted in a rigid baffle of infinite extent. (a) Magnitude. (b) Phase.

For the phase shown in Figure 9b, a good agreement is observed between the two models for frequencies below about 100 kHz. Above 100 kHz, the phase of the SFDC model increases and the deviation is 35° at 210 kHz. They intersect at 214 kHz, and the SFDC is 60° below Khimunin's model at 220 kHz. As the frequency increases, the deviation between the models decreases and the two models follow the same trend between $250 - 350$ kHz, with the SFDC approximately 15° below Khimunin's model.

Figure 10 shows the magnitude and phase of the diffraction correction H^{diff} for the baffled element (as shown in Figure 9), along with the magnitude and phase of the average pressure $\langle p \rangle$ and the equivalent plane wave pressure $p^{eq,plane}$, all at $z = 15$ cm, which are used to calculate the diffraction correction, cf. Eq. 8.

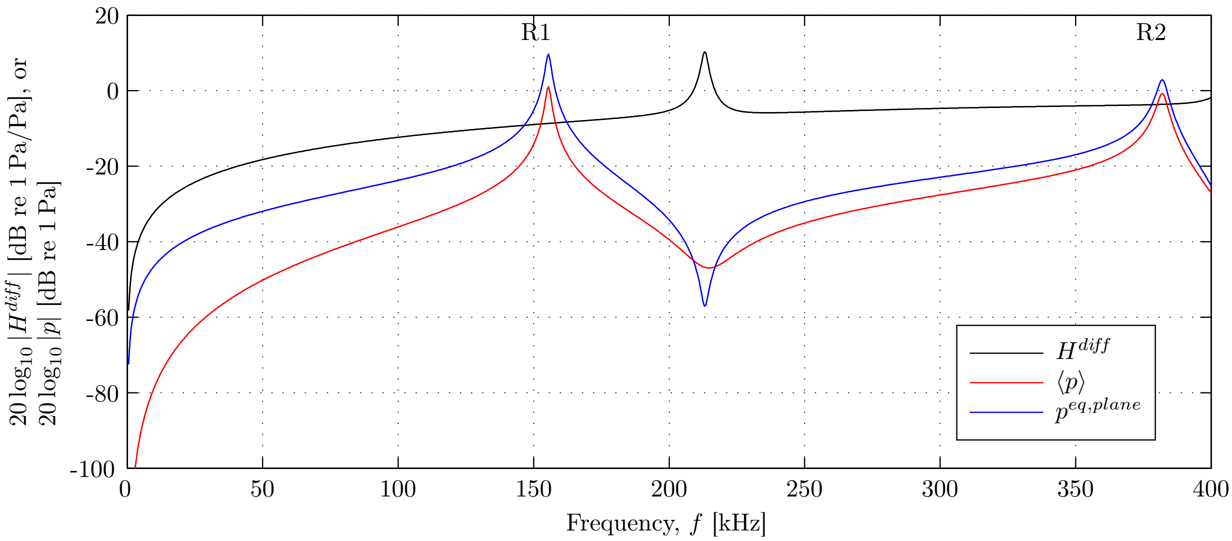

(a)

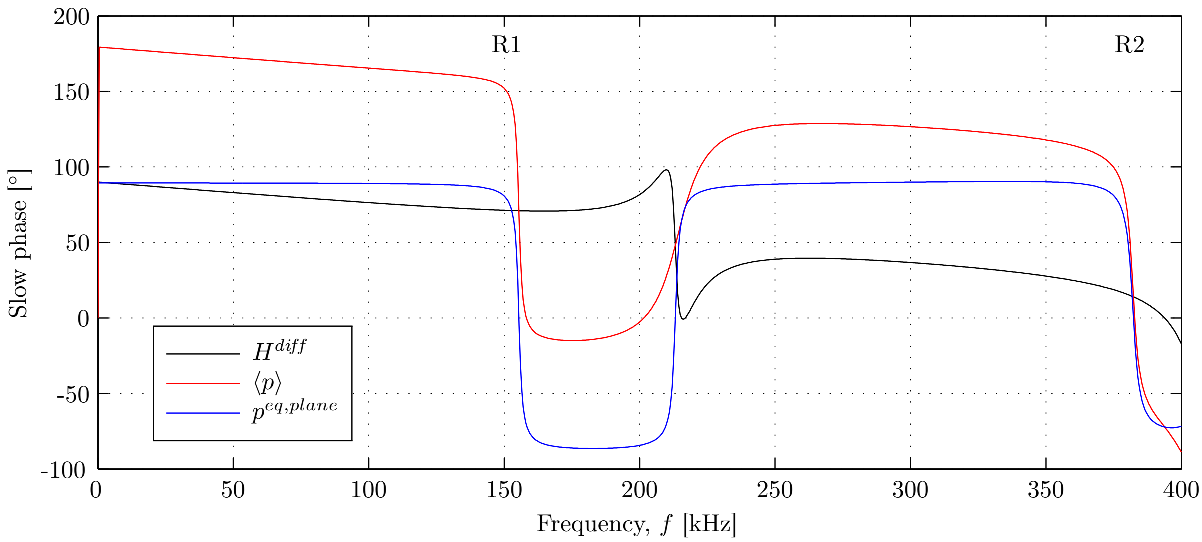

(b)

Figure 10: SFDC calculated diffraction correction H^{diff}, shown together with the average pressure $\langle p\rangle$ and the equivalent plane wave pressure, $p^{eq,plane}$, both at $L = 15$ cm, for the piezoceramic element mounted in a rigid baffle of infinite extent. (a) Magnitude. (b) Slow phase.

In Figure 10a, the magnitude of $p^{eq,plane}$ is consequently larger than the magnitude of $\langle p\rangle$, except in the region of the peak in the diffraction correction at 214 kHz. Since $\langle p\rangle$ is calculated at 15 cm, some near-field effects may be present around 214 kHz, in addition to the averaging of the pressure, causing the pressure "dip" to be reduced in depth relative to in the far-field. Since the equivalent plane wave pressure is found by extrapolating the on-axis far-field pressure at 1000 m back to the source, near-field effects are not present in $p^{eq,plane}$, cf. Section 2.6, causing the "sharp" dip of $p^{eq,plane}$ at 214 kHz, and hence in turn the peak in the diffraction correction. The subtraction of the two phase responses results in the phase response of H^{diff}, shown in the figure.

In Figure 10b, the phase of the average pressure $\langle p\rangle$ starts at 180° and decreases in a linearly manner as the frequency increases. A phase shift is observed between 150 kHz and 230 kHz, which is ascribed to the transducer response around and above the first radial mode R1. A similar behaviour is observed near the second radial mode, R2. The phase of $p^{eq,plane}$ starts at 90°, and does not have a decrease with increasing frequency, which the phase of the average pressure does. This reveals the far-field phase response of the transducer, since $p^{eq,plane}$ is calculated by extrapolating back from 1000 m. A phase shift of 180° in the region of the first radial mode is also observed as for $\langle p \rangle$.

As discussed above, the transducer response vanishes in the SFDC method. This can be observed in Figure 10a where the magnitude peaks in $\langle p \rangle$ and $p^{eq,plane}$ at the first and second radial modes at 155.5 kHz and 382 kHz, are not present in the magnitude of the diffraction correction. Similarly, the 180° phase shift between 155.5 kHz and 214 kHz associated with the transducer response, is not present in the phase of the diffraction correction.

Figure 11 shows the magnitude and phase of the diffraction correction for the unbaffled piezoceramic element, calculated with Khimunin's model and the SFDC.

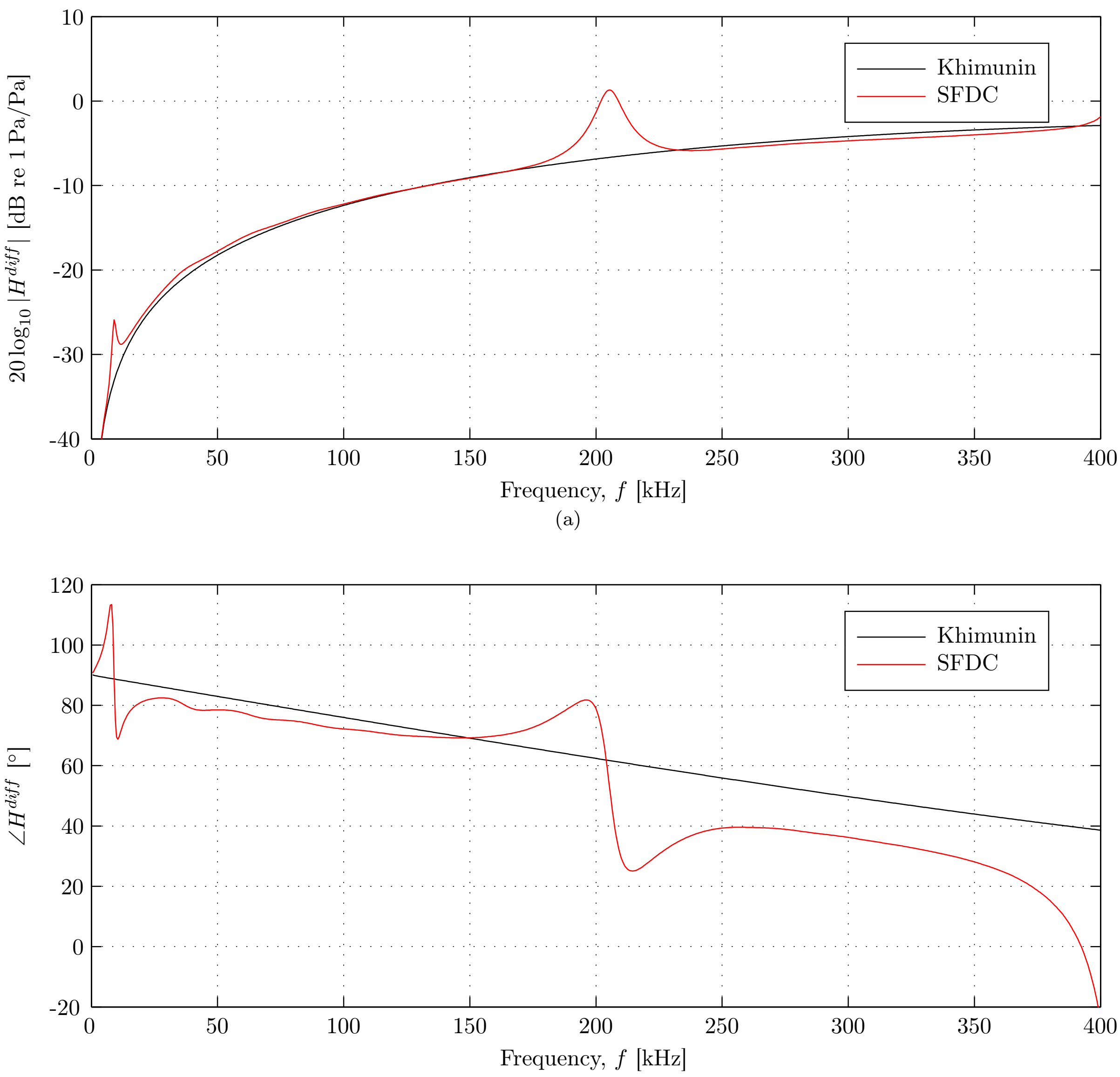

Figure 11: Comparison of the diffraction correction H^{diff} as a function of frequency, calculated using Khimunin's model and the SFDC, for the Pz27 piezoceramic element ($D = 12.7$ mm, $T = 2$ mm) vibrating and radiating in air. (a) Magnitude. (b) Phase.

For the magnitude shown in Figure 11a, a similar trend is observed as in Figure 9, when the piezoceramic element is placed in the rigid baffle of infinite extent. However, as compared with the baffled element, the magnitude of the peak of the SFDC is 8 dB lower, reducing the deviation compared with Khimunin's model, and the frequency is shifted down to 205 kHz. The deviation for frequencies above 230 kHz is about the same as for the baffled element shown in Figure 9a, but there is a deviation compared with Khimunin's model for frequencies below 100 Hz. A significant peak in the magnitude of H^{diff} calculated with the SFDC is also observed at 9 kHz. This peak is caused by the "dip" in the source sensitivity seen in Figure 8, and the overall deviation in this frequency region may be caused by the undulations discussed in Section 3.1, i.e. interference from the sides and possibly the rear surface of the element.

For the phase in Figure 11b, the same overall behaviour as for the baffled element is present, in addition to the deviations due to undulations, as discussed for the magnitude above. The phase deviation from Khimunin's model between $150 - 250$ kHz is reduced compared to the baffled element, with a deviation of 20° at 196 kHz, and 35° at 214 kHz. The phase responses using the two models cross at a lower frequency than for the baffled piezoceramic element, at 205 kHz.

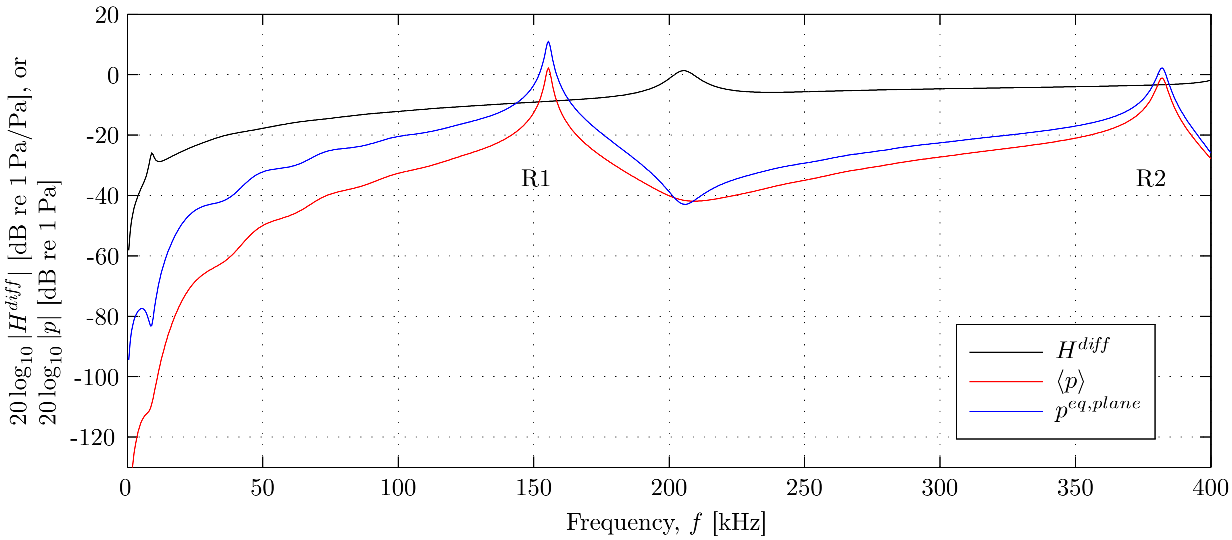

(a)

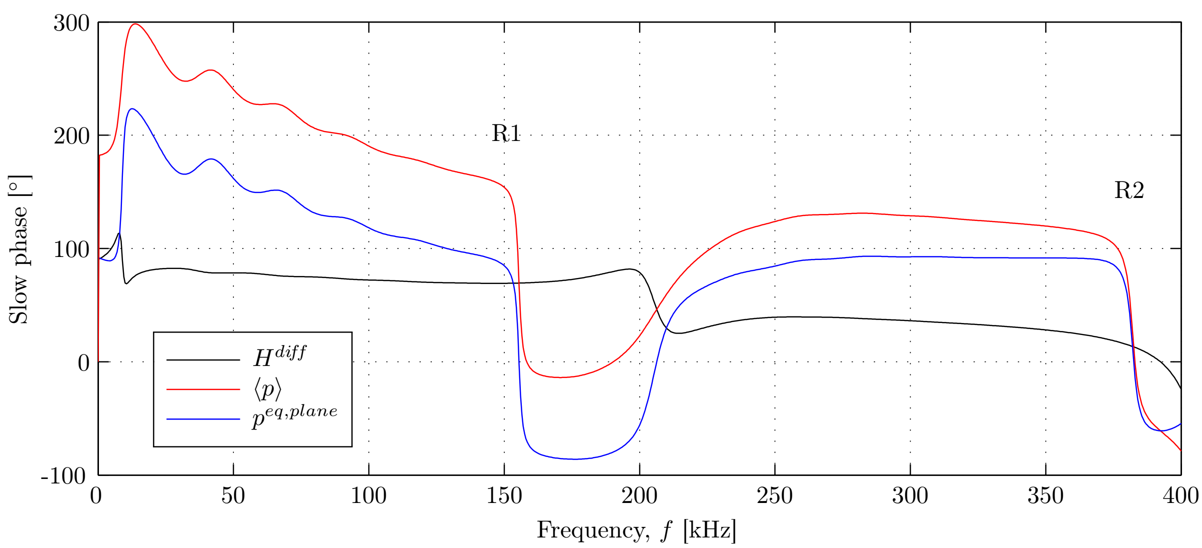

(b)

Figure 12: The diffraction correction H^{diff} compared with the average pressure $\langle p \rangle$ and the equivalent plane wave pressure, $p^{eq,plane}$, all at $z = 15$ cm, for the piezoceramic element without a baffle. (a) Magnitude. (b) Slow phase.

Figure 12 shows the magnitude and phase of the diffraction correction H^{diff} for the unbaffled element (as shown in Figure 11), along with the magnitude and phase of the average pressure $\langle p \rangle$ and the equivalent plane wave pressure $p^{eq,plane}$, which are used to calculate H^{diff}, cf. Eq. 8. The magnitudes shown in Figure 12 exhibit the same characteristics as for the baffled element, seen in Figure 10. However, undulations are present in all the curves for frequencies below 100 kHz. The undulations in H^{diff} are not as large for $\langle p \rangle$ as for $p^{eq,plane}$. This is seen e.g. at the peak in the magnitude of the diffraction correction at 9 kHz, where the equivalent plane wave pressure $p^{eq,plane}$ has a more distinct dip at 9 kHz. The average pressure $\langle p \rangle$ does not show such a dip.

The phase shown in Figure 12b also has the same characteristics as for the baffled element shown in Figure 10b, but there is a large "jump" in the phase for low frequencies, which is likely to be a consequence of the undulations. Similar jumps are present for both the average pressure $\langle p \rangle$ and the equivalent plane wave pressure $p^{eq,plane}$, so the resulting phase in the diffraction correction is not so dramatically affected, except for the peak and dip around 9 kHz, assumed to be caused by differences in the phase jump of $\langle p \rangle$ and $p^{eq,plane}$.

For comparison, Figure 13 shows the magnitude and phase of the SFDC calculated diffraction corrections for the baffled and unbaffled piezoceramic element, respectively. These are the same as shown in Figure 9 and 10, and 11 and 12, respectively. Figure 13 thus shows the effect of the baffle on the diffraction correction for the piezoceramic element. By mounting the piezoceramic element in a rigid baffle of infinite extent, the peak at 205 kHz for the unbaffled element is shifted to 214 kHz, and the magnitude of the peak is increased. This increase in magnitude also causes a larger deviation from Khimunin's model at 214 kHz compared to at 205 kHz. The undulations in the diffraction correction, for both the magnitude and phase, for lower frequencies, i.e. below 100 kHz, are not observed when the element is baffled, In this frequency range, a good agreement between the SFDC is found. The baffle has the same effect on the phase of the diffraction correction; the undulations for lower frequencies are not observed, the deviation near the peak in the magnitude increases, and there is a upwards shift in frequency.

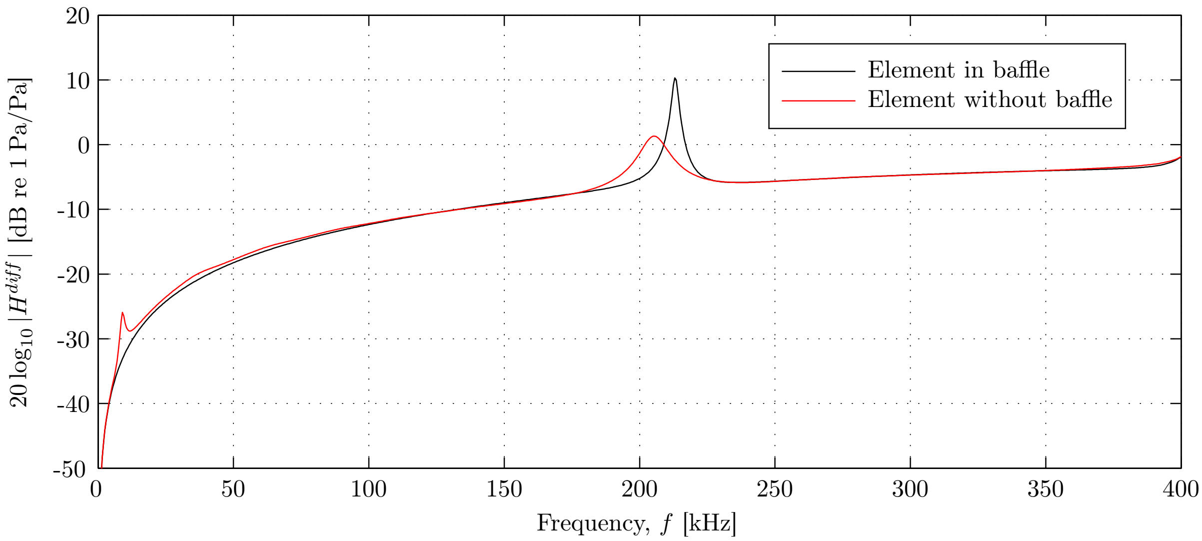

(a)

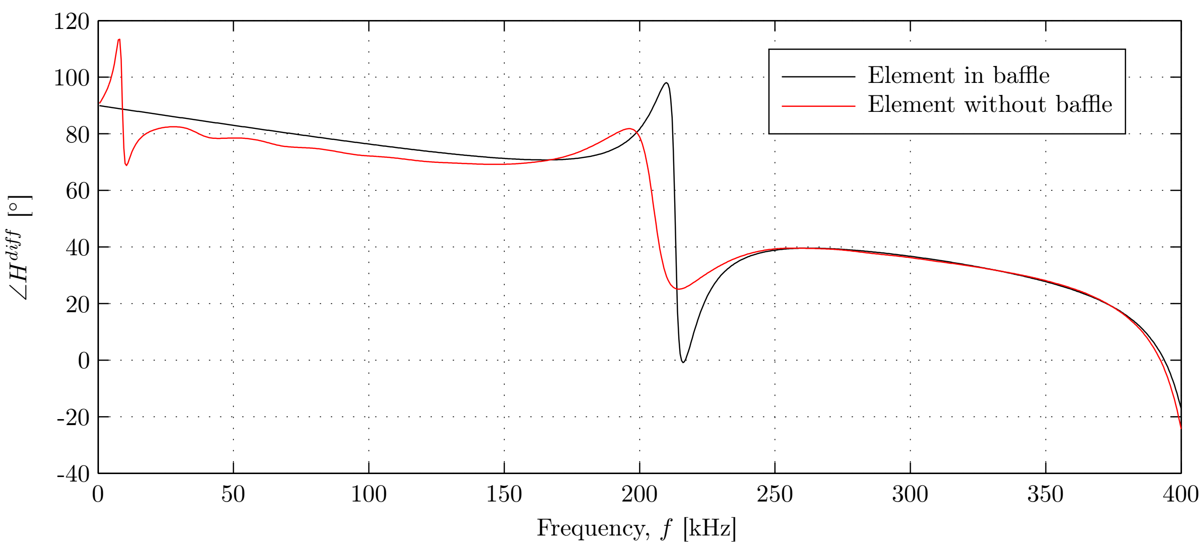

(b)

Figure 13: Comparison of the diffraction corrections calculated with the SFDC, for a piezoelectric element mounted in a baffle and without a baffle, respectively. (a) Magnitude. (b) Slow phase.

In order to study the diffraction correction for the unbaffled element, certain frequencies have been selected from Figure 11a for further analysis. Points where there are large deviations between the calculations with Khimunin's model and the SFDC, points where there is good agreement, and the first and second radial modes of the piezoceramic element, have been selected. Table 1 shows a comparison of the magnitude and phase of the SFDC compared with Khimunin's model, along with the tentative required uncertainty in the diffraction correction, calculated according to Eq. 11.

Table 1: Comparison of diffraction correction model calculations for selected frequencies, for the unbaffled piezoceramic element. The difference between Khimunin's model and the SFDC method is given for the magnitude and phase. The phase differences in degrees are converted to time difference. Calculated tentative uncertainty requirements for the phase of H^{diff} in the phase, are given according to Eq. (11). Note that $u(\angle H^{diff})$ is for information only and should not be compared with t^{diff}, since t^{diff} relates to the comparison between Khimunin's model and the SFDC method, and the "true value" is not known.

Frequency [kHz]	Difference			$u(\angle H^{diff})$ [°]
	$20\log_{10}\lvert H^{diff}\rvert$ [dB]	$\angle H^{diff}$ [°]	t^{diff} [µs]	
9.0	-7.2	-0.6	0.18	0.03
50.0	-0.5	4.5	0.25	0.16
155.5	0.1	-1.0	-0.02	0.49
205.0	-7.1	24.6	0.33	0.65
300.0	0.5	13.5	0.13	0.95
382.0	0.3	26.9	0.20	1.20

3.3. Discussion of the deviations in the diffraction correction calculations

Figure 14-19 shows the radiated beam pattern, the displacement of the Pz27 element (exaggerated for illustration purposes), and the pressure field (when the element is exited with 1 V), calculated using FEM for selected frequencies shown in Table 1. The beam pattern calculated with FEM is compared to that of the plane piston model [24], where the beam pattern is scaled to the axial pressure. Here, a slightly different approach is used for the FEM results since the side lobe pressures in some cases are higher than the axial pressure. Hence, the beam pattern calculated with FEM is scaled to the maximum value over the presented angular range, not the axial pressure.

The pressure field is presented for the axial distance $0\,\text{cm} \leq z \leq 16\,\text{cm}$, and the lateral distance $-3\,\text{cm} \leq r \leq 3\,\text{cm}$. A "receiver", with identical dimensions as the transmitter, is placed in the location described in Section 3.1. This is purely for illustrative purposes, as no receiver is present in the simulations of the pressure field. The average pressure $\langle p \rangle$ used in the diffraction correction, is calculated in the fluid over the "measurement area" at the position of the front face of this receiver, in absence of the receiver.

The unbaffled piezoceramic element at 9 kHz

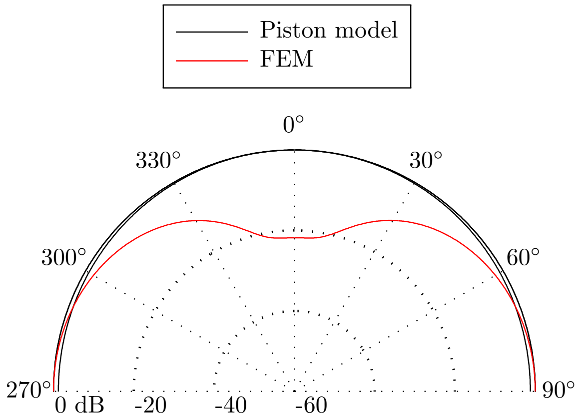

(a)

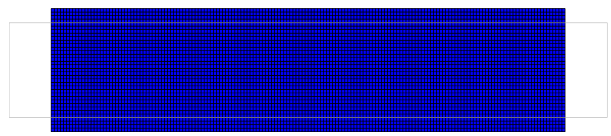

(b)

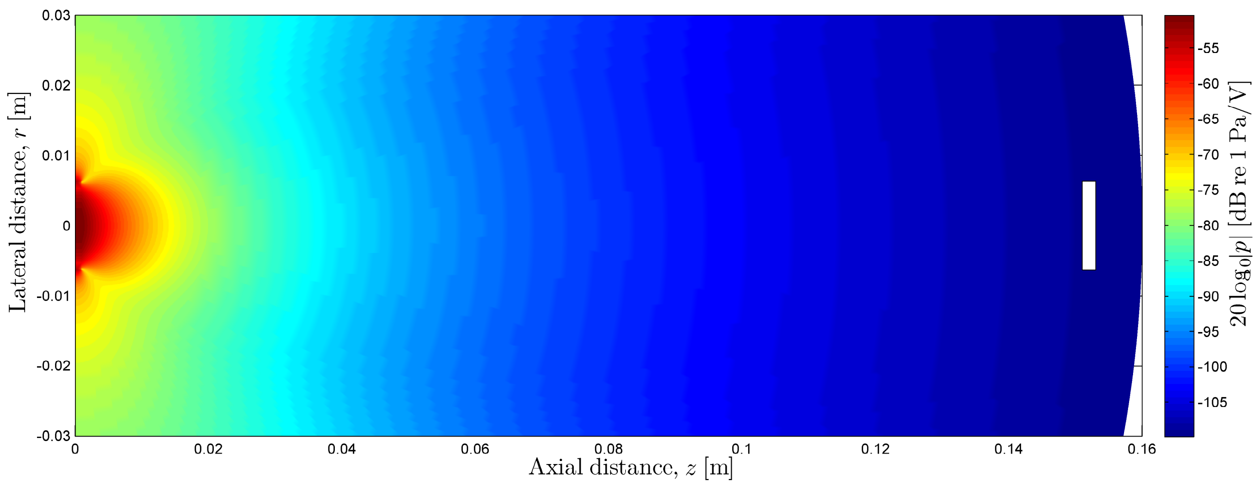

(c)

Figure 14: Finite element calculations of the unbaffled piezoceramic element's vibration and radiated sound field in air at 9 kHz, for $a = 6.35$ mm (i.e. $ka \approx 1$). The Rayleigh distance is 3.3 mm. (a) Far-field beam pattern at 1 m, compared with the piston model with equal radius. (b) Vibrational displacement. (c) Sound pressure field in the near field and the transition to the far-field.

At 9 kHz (Fig. 14), the magnitude of the diffraction correction calculated with the SFDC deviates with -7.2 dB from Khimunin's model, and the phase deviation is $-0.6°$, as seen in Table 1. At the axis, a flat region is observed for the FEM model. This is causing the "dip" at 9 kHz in the source sensitivity for the unbaffled element, shown in Figure 8. This "dip" may, as discussed in Section 3.1, be caused by interference from the sides and the rear surface of the element. The front surface of the element has a piston-like movement, i.e. uniform vibration across the surface, and there is also a large radial movement. In the pressure field there is no distinct main lobe, except for near the front surface.

The unbaffled piezoceramic element at 50 kHz

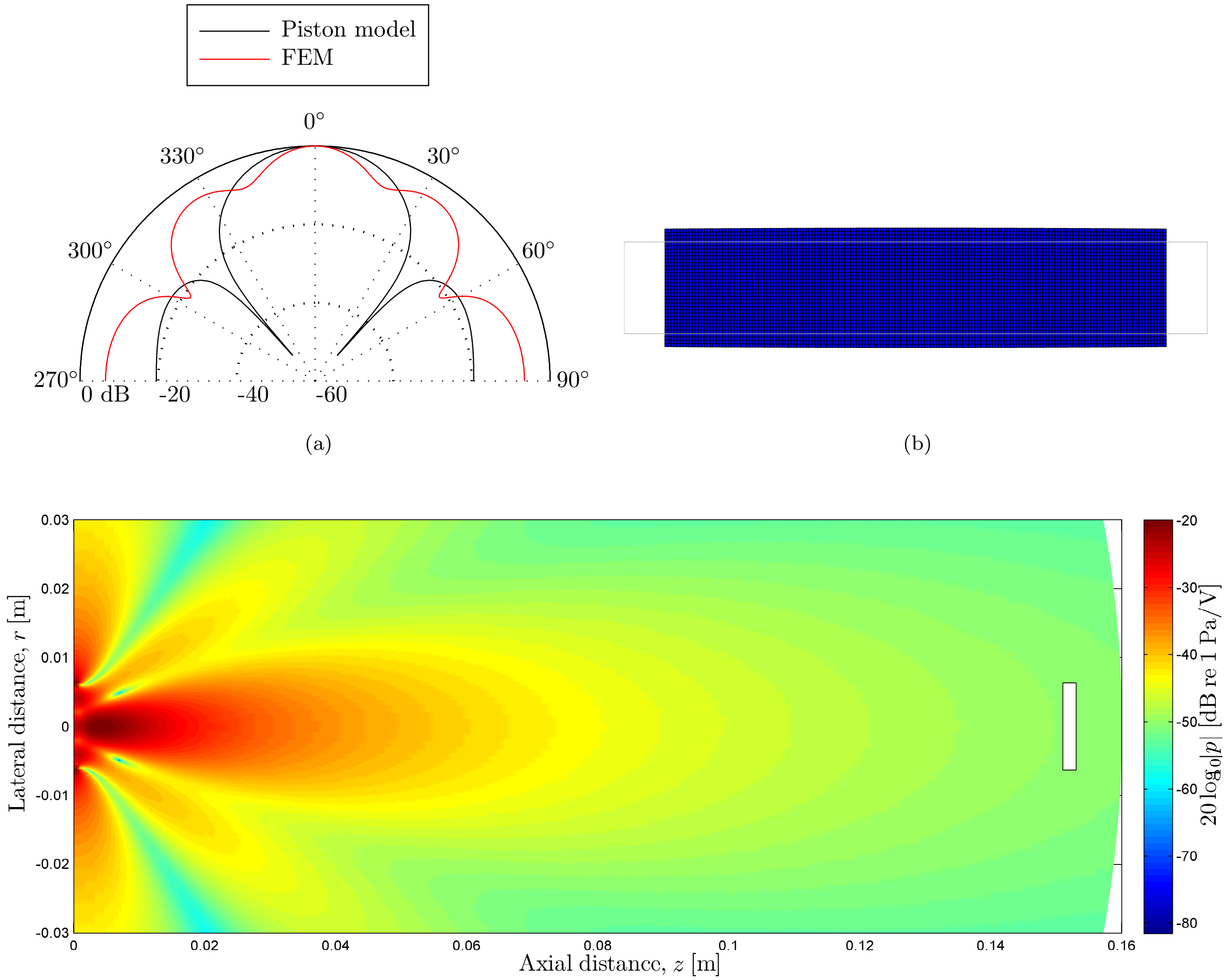

(c)

Figure 15: Finite element calculations of the unbaffled piezoceramic element's vibration and radiated sound field in air at 50 kHz, for $a = 6.35$ mm (i.e. $ka \approx 6$). The Rayleigh distance is 1.8 cm. (a) Far-field beam pattern at 1 m, compared with the plane piston model. (b) Vibrational displacement. (c) Sound pressure field in the near field and the transition to the far-field.

At 50 kHz (Fig. 15), still below R1, the magnitude and phase of H^{diff} calculated with the SFDC agrees with Khimunin's model within -0.5 dB and $4.5°$, as seen in Table 1. The beam pattern presented in Figure 15a shows that the piston model has a wide main lobe and a distinct side lobe, while the beam pattern calculated with FEM for the unbaffled element has a more narrow main lobe and two side lobes. The displacement in Figure 15b is very similar to the displacement for 9 kHz, i.e. a piston-like movement of the front surface and strong radial vibration. The pressure field in Figure 15c shows the large radiation to the sides, along with the wide main lobe.

The unbaffled piezoceramic element at 155.5 kHz

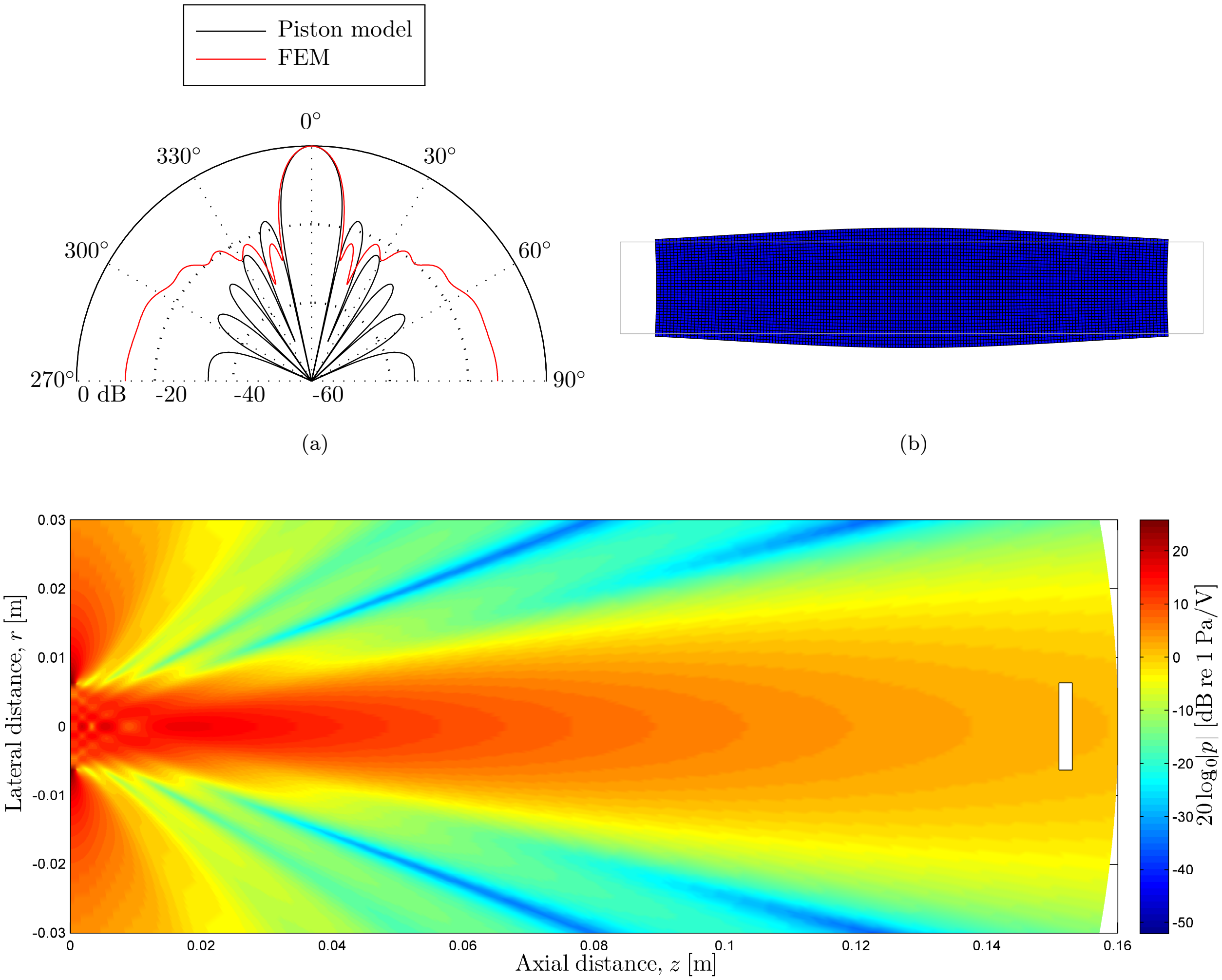

(c)

Figure 16: Finite element calculations of the unbaffled piezoceramic element's vibration and radiated sound field in air at 155.5 kHz, for $a = 6.35$ mm (i.e. $ka \approx 18$). The Rayleigh distance is 5.7 cm. (a) Far-field beam pattern at 1 m, compared with the plane piston model. (b) Vibrational displacement. (c) Sound pressure field in the near field and the transition to the far-field.

At 155.5 kHz (Fig. 16), the first radial mode of the piezoceramic element (R1), both the magnitude and phase of the diffraction correction, calculated with the SFDC, are in agreement with Khimunin's model. The deviation in magnitude is 0.1 dB and the deviation in phase is $-1°$, cf. Table 1. The main lobe is similar to the piston model. The direction of the first side lobe corresponds well with the piston model, with a lower magnitude, but the piezoceramic element has a larger radiation to the sides than the piston model. The displacement is curved along the surface of the element, both on the front and at the sides of the element. The sound pressure field has a very distinct main lobe which dominates the field, together with a high level of side radiation.

The unbaffled piezoceramic element at 205 kHz

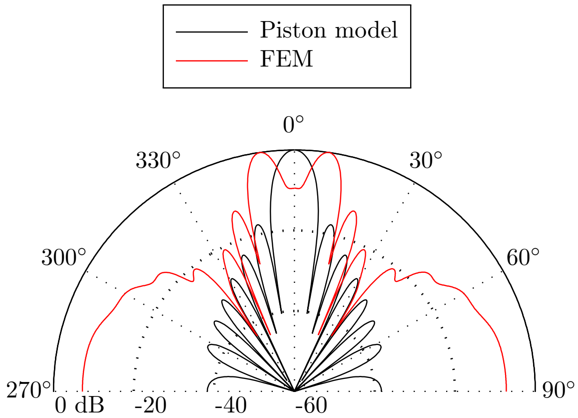

(a)

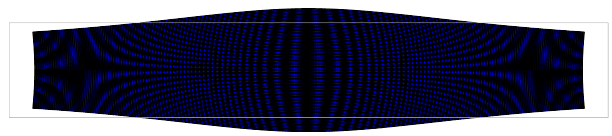

(b)

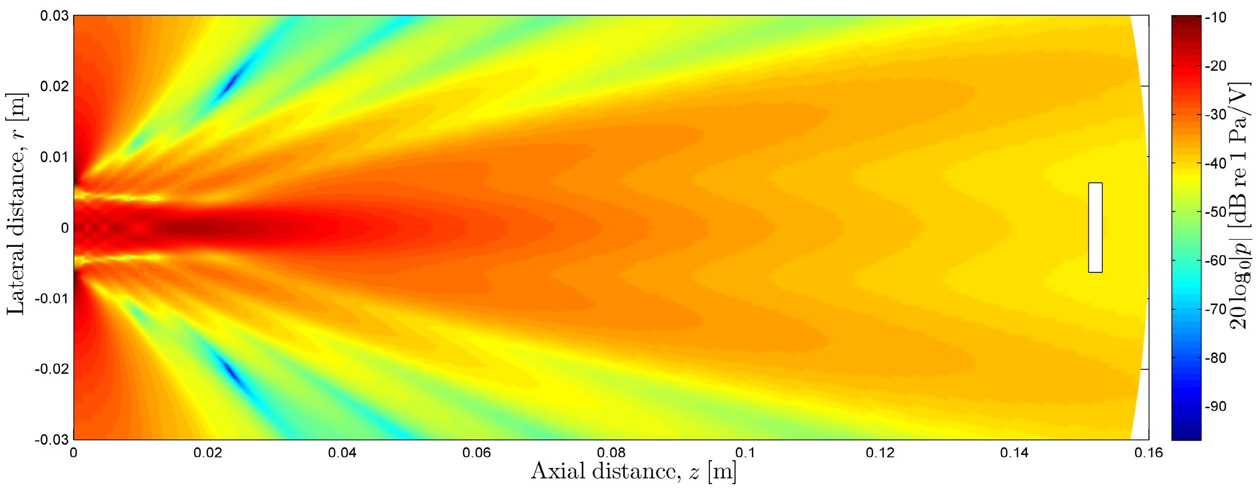

(c)

Figure 17: Finite element calculations of the unbaffled piezoceramic element's vibration and radiated sound field in air at 205 kHz, for $a = 6.35$ mm (i.e. $ka \approx 24$). The Rayleigh distance is 7.6 cm. (a) Far-field beam pattern at 1 m, compared with the plane piston model. b) Vibrational displacement. (c) Sound pressure field in the near field and the transition to the far-field.

At 205 kHz (Fig. 17), which corresponds to the "dip" in S_V shown in Figure 8 for the unbaffled element, a deviation of -7.1 dB and 24.6° in the diffraction correction is observed between the SFDC and Khimunin's model, as seen in Table 1. The beam pattern calculated with FEM has two high side lobes and no lobe along the axis. The shape of the displacement reveals a nodal ring at the front surface, causing the front surface to expand and retract at the same time across the surface. The pressure field illustrates the high side lobes, but at 15 cm distance there is also a small main lobe at the z-axis, which is not present in the beam pattern at 1 m, cf. Figure 17a.

The unbaffled piezoceramic element at 300 kHz

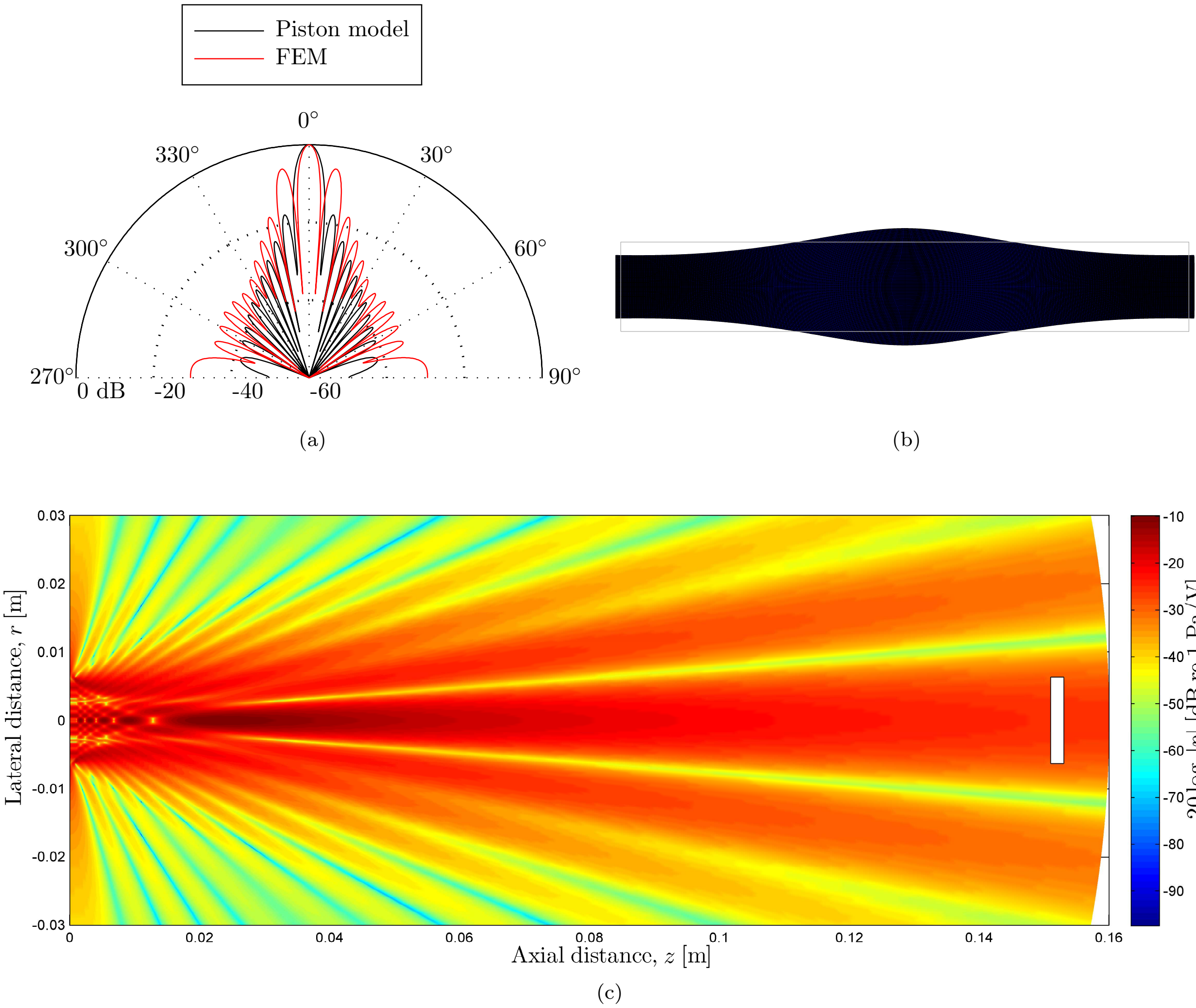

Figure 18: Finite element calculations of the unbaffled piezoceramic element's vibration and radiated sound field in air at 300 kHz, for $a = 6.35$ mm (i.e. $ka \approx 35$). The Rayleigh distance is 11.1 cm. (a) Far-field beam pattern at 1 m, compared with the plane piston model. (b) Vibrational displacement. (c) Sound pressure field in the near field and the transition to the far-field.

At 300 kHz (Fig. 18), well above the first radial mode, the magnitude of the diffraction correction calculated with the SFDC, is in good agreement with the Khimunin calculations, within 0.5 dB, and the phase deviation is 13.5°, as seen in Table 1. The main lobe of the beam pattern calculated with FEM corresponds fair with the piston model. The first side lobe is very high, especially compared to the piston model. The rest of the side lobes are very low compared to those in Figure 14-17. The vibrational pattern is similar to the one at 205 kHz, but the node is close to the centre of the disk, and the vibration to the sides is not so large. This may be the reason for the low side lobes in Figure 18a. The pressure field illustrates the many side lobes and that the first side lobes are very high. The receiver is located entirely within the main lobe.

The unbaffled piezoceramic element at 382 kHz

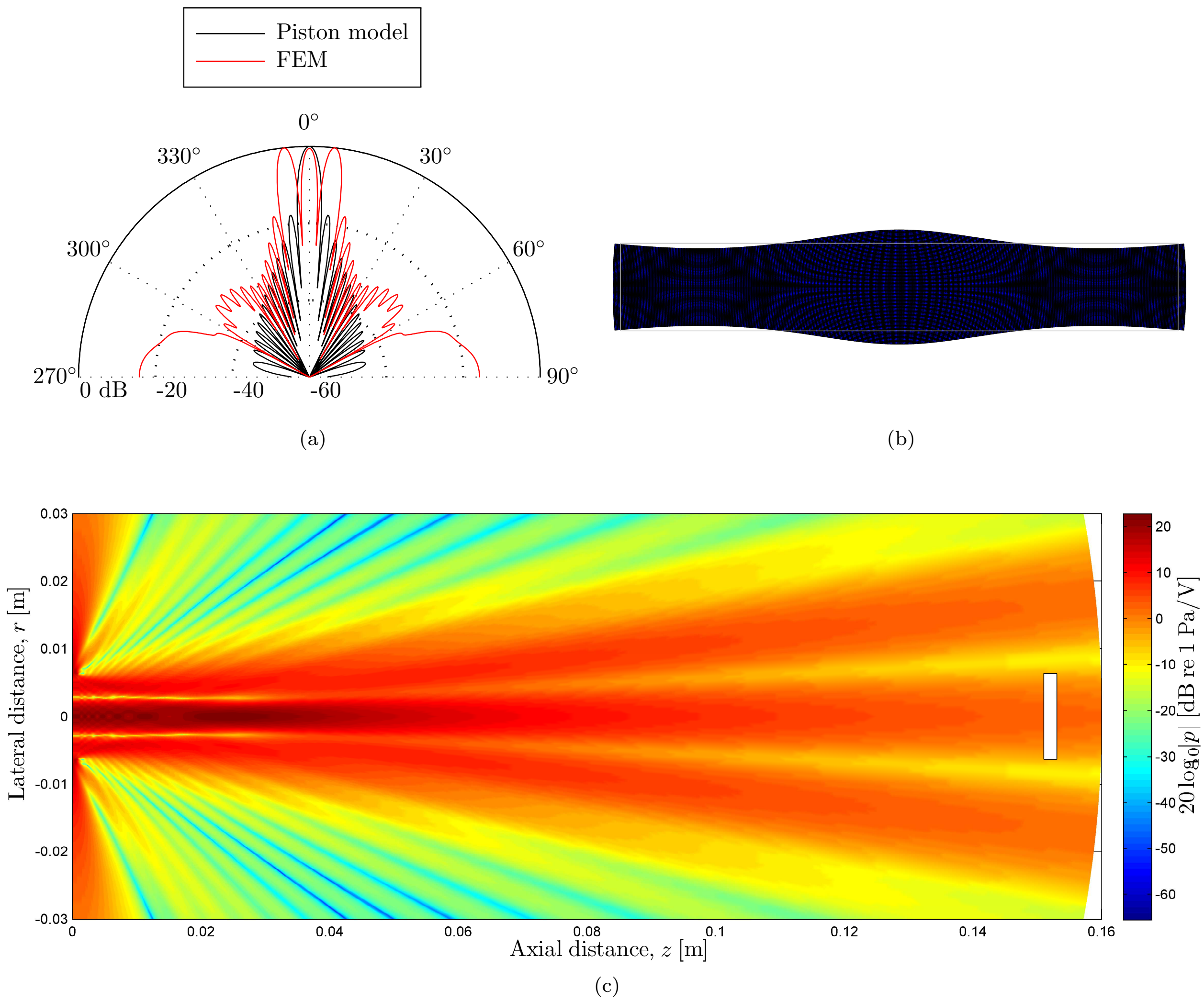

Figure 19: Finite element calculations of the unbaffled piezoceramic element's vibration and radiated sound field in air at 382 kHz, for $a = 6.35$ mm (i.e. $ka \approx 44$). The Rayleigh distance is 14.1 cm. (a) Far-field beam pattern at 1 m, compared with the plane piston model. (b) Vibrational displacement. (c) Sound pressure field in the near field and the transition to the far-field.

At 382 kHz (Fig. 19), the second radial mode of the piezoceramic element (R2), the deviation in magnitude of the diffraction correction calculated with the SFDC compared to Khimunin is 0.3 dB, and the phase deviation is 26.9°, as seen in Table 1. The beam pattern calculated with FEM shows that the main lobe is similar to the piston model, but the side lobes are higher for the piezoceramic element. The displacement vibration has a second node on the surface, resulting in the higher radiation to the sides as seen in the beam pattern. The pressure field again illustrates the many side lobes, and the high first side lobe level. The diameter of the receiver is almost equal to the beam width of the main lobe at 15 cm.

4. Conclusions

To explore and aid in our understanding of the diffraction correction properties for real piezoelectric transducers and their vibration modes, the complex mechanisms involved are analyzed by considering a simplified transducer construction, a circular piezoceramic disk element vibrating in air. The diffraction correction for such a piezoceramic element is studied using a simplified finite element diffraction correction method (SFDC), including comparison with the conventional uniform piston diffraction correction model introduced by Williams and Khimunin. Various grades of complexity are introduced gradually, from the level of the uniform piston diffraction correction model, to analyze the various effects appearing in the diffraction correction of a piezoceramic disk, over a frequency range covering the important first and second radial modes of the disk element, R1 and R2, respectively.

Significant deviations are found for the SFDC calculated diffraction correction as compared with the conventional uniform piston diffraction correction model. The deviations are especially large in the frequency region of the source sensitivity minimum which appears in the far field above the R1 mode. For the phase the deviation is significant for all frequencies above the R1 mode. Further analysis is required to fully explain the deviations found for the piezoceramic disk in these regions, between the SFDC calculated diffraction correction, and the conventional model.

In addition, significant undulations are observed in the magnitude and phase of the diffraction correction of the piezoceramic disk, over a wide frequency band covering very low frequencies to above the R1 mode. The undulations are strongest at low frequencies. The analysis of an unbaffled vs. a baffled element indicates that these undulations are caused by radiation from the sides and possibly the rear of the disk element, interfering with the waves radiated from the front of the element. These undulations are not described by the uniform piston diffraction correction model.

Correction for ultrasonic transducer diffraction effects is discussed and evaluated in relation to realizing a precision sound velocity cell within $100-200\,\text{ppm}$ relative uncertainty (95 % conf. level), for use in custody transfer energy measurement of natural gas at elevated pressures. In this application, for relevant measurement methods at laboratory conditions, the diffraction correction phase might preferably be known within $0.5°$, tentatively, in the $150-200\,\text{kHz}$ operational frequency range of ultrasonic multipath fiscal flow meters. For actual transducers in such applications, the results of the study strongly indicate that traditional diffraction correction models based on the "piston model" are not sufficiently accurate over the frequency band of interest.

A challenge at the present stage of the study is the fact that a “true value” of the diffraction correction for a piezoceramic disk has not been available, so that the accuracy of the SFDC model (such as in relation to the tentative requirement stated above) could not be evaluated. Based on accumulated experience with the finite element model used, including comparison with measurements and other full-wave models, it is however expected that for a piezoceramic disk the SFDC approach represents a more accurate description than the uniform piston diffraction correction model. In this approach, a full description of the transmitting transducer and the radiated sound field is accounted for, including radiation at the sides and rear of the transducer, and non-uniform vibration. However, the SFDC method does not account for the full diffraction effects at the receiving transducer, such as reception at the sides and rear of the transducer.

Work is in progress experimentally and theoretically to include also a full description of the receiver, to obtain a more complete description and treatment of the diffraction effects. The relatively simple case of a piezoceramic disk element as well as more complex transducer constructions are relevant objects for analysis in this context.

Acknowledgements

The present work is made as part of a PhD-project (2009-12) for the first author, “High-precision sound velocity cell technology for gas characterization”, in a cooperation between the Michelsen Centre for Industrial Measurement Science and Technology, the University of Bergen (UiB), Dept. of Physics and Technology, Christian Michelsen Research AS (CMR) and FMC Technologies Ltd. The project is financed through the Michelsen Centre for Industrial Measurement Science and Technology, by The Research Council of Norway (NFR) and Statoil ASA.

References

[1] P. Lunde and M. Vestrheim, “Precision sound velocity cell for natural gas at high pressures. Phase 1 - feasibility study.”, CMR Report no. CMR-98-F10039 (Confidential), Christian Michelsen Research AS, Bergen, Norway (1998).

[2] P. Norli and P. Lunde, “A Three-Way Pulse Method for a Precision Sound Velocity Measurement Cell”, in *Proceedings of the 2006 IEEE Ultrasonics Symposium, Vancouver, Canada, 3-6 October, 2006*, 888–893 (2006).

[3] P. Lunde, P. Norli, M. Vestrheim, and R. A. Kippersund, “Precision sound velocity cell as reference for gas quality measurement in ultrasonic flow meters. Preliminary results using two candidate methods with argon at low pressure”, in *Proceedings of the 30th Scandinavian Symposium on Physical Acoustics, Geilo, Norway, January 28-31, 2007* (2007).

[4] P. Norli, “Sound velocity cell for gas characterization”, PhD thesis, Department of Physics and Technology, University of Bergen, Bergen, Norway (2007).

[5] C. D. Reid, “Some investigations into the velocity of sound at ultra-sonic frequencies using quartz oscillators”, Physical Review **35**, 814–831 (1930).

[6] C. D. Reid, “Notes on the effect of distance from the source on the velocity of sound at ultrasonic frequencies”, Physical Review **37**, 1147–1148 (1931).

[7] M. Grabau, “A Study of the Velocity of Sound in Air”, J. Acoust. Soc. Am. **5**(1), 1–9 (1933).

[8] W. J. Fry, “The Double Crystal Acoustic Interferometer”, J. Acoust. Soc. Am. **21**(1), 17–28 (1949).

[9] H. Seki, A. Granato, and R. Truell, “Diffraction Effects in the Ultrasonic Field of a Piston Source and Their Importance in the Accurate Measurement of Attenuation”, J. Acoust. Soc. Am. **28**(2), 230–238 (1956).

[10] A. O. Williams Jr., “The Piston Source at High Frequencies”, J. Acoust. Soc. Am. **23**(1), 1–6 (1951).

[11] A. S. Khimunin, “Numerical Calculation of the Diffraction Corrections for the Precise Measurement of Ultrasound Absorption”, Acustica **27**, 173–181 (1972).

[12] A. S. Khimunin, “Numerical Calculation of the Diffraction Corrections for the Precise Measurement of Ultrasound Phase Velocity”, Acustica **32**, 192–200 (1975).

[13] A. S. Khimunin, “Ultrasonic parameter measurements incorporating exact diffraction corrections”, Acustica **39**, 87–95 (1978).

[14] E. P. Papadakis, “Correction for Diffraction Losses in the Ultrasonic Field of a Piston Source”, J. Acoust. Soc. Am. **31**(2), 150–152 (1959).

[15] H. J. McSkimin, “Empirical Study of the Effect of Diffraction on Velocity of Propagation of High-Frequency Ultrasonic Waves”, J. Acoust. Soc. Am. **32**(11), 1401–1404 (1960).

[16] K. Yamada and Y. Fujii, “Acoustic Response of a Circular Receiver to a Circular Source of Different Radius”, J. Acoust. Soc. Am. **40**(5), 1193–1194 (1966).

[17] E. P. Papadakis, “Ultrasonic Phase Velocity by the Pulse-Echo-Overlap Method Incorporating Diffraction Phase Corrections”, J. Acoust. Soc. Am. **42**(5), 1045–1051 (1967).

[18] M. B. Gitis and A. S. Khimunin, “Diffraction effects in ultrasonic measurements”, Sov. Phys. Acoust. **14**(4), 413–431 (1969).

[19] E. P. Papadakis, “Ultrasonic diffraction loss and phase change for broad-band pulses”, J. Acoust. Soc. Am. **53**(3, Pt.2), 847–849 (1972).

[20] K. Beissner, “Exact Integral Expression for the Diffraction Loss of a Circular Piston Source”, Acustica **49**, 212–217 (1981).

[21] P. Lunde, K.-E. Frøysa, R. Kippersund, and M. Vestrheim, “Transient diffraction effects in ultrasonic meters for volumetric, mass and energy flow measurement of natural gas”, in *Proceedings of the 21st North Sea Flow Measurement Workshop, Tønsberg, Norway, 28-31 October 2003* (2003).

[22] P. Lunde, K.-E. Frøysa, and M. Vestrheim, “Transient diffraction effects on ultrasonic flow meters for gas and liquid”, in *Proceedings of the 26th Scandinavian Symposium on Physical Acoustics, Ustaoset, Norway, 26-29 January 2003* (2003).

[23] P. Lunde, R. A. Kippersund, M. Vestrheim, and K.-E. Frøysa, "Transient diffraction effects in piezoelectric ultrasonic transducers using finite element modelling", in *Proceedings of the 27th Scandinavian Symposium on Physical Acoustics, 25-28 January, 2004, Ustaoset, Norway* (2004).

[24] L. E. Kinsler, A. R. Frey, A. B. Coppens, and J. V. Sanders, *Fundamentals of Acoustics*, 4th edition (John Wiley & Sons, New York) (2000).

[25] J. Kocbach, "Endelig Element Modellering av Piezoelektriske Skiver", Master thesis, Department of Physics, University of Bergen, Bergen, Norway (1996).

[26] J. Kocbach, "Finite Element Modeling of Ultrasonic Piezoelectric Transducers", PhD thesis, Department of Physics, University of Bergen, Bergen, Norway (2000).

[27] J. Kocbach, P. Lunde, and M. Vestrheim, "Resonance frequency spectra with convergence tests of piezoceramic disks using the finite element method", Acta Acustica united with Acustica **87**, 271–285 (2001).

[28] J. Kocbach, P. Lunde, M. Vestrheim, and R. Kippersund, "Finite element modeling of ultrasonic piezoelectric transducers: Extension of FEMP to 3D analysis.", CMR Report no. CMR-06-A10046-RA-01, Christian Michelsen Research AS, Bergen, Norway (December 2006).

[29] K.-E. Frøysa and P. Lunde, "Density and calorific value measurement in natural gas using ultrasonic flow meters", in *Proceedings of the 23rd International North Sea Flow Measurement Workshop, Tønsberg, Norway, 18-21 October 2005* (2005).

[30] K.-E. Frøysa, P. Lunde, A. Paulsen, and E. Jacobsen, "Density and calorific value measurement of natural gas using ultrasonic flow meters. Results from testing on various North Sea gas field data.", in *Proceedings of the 24th International North Sea Flow Measurement Workshop, St. Andrews, Scotland, 24-27 October 2006* (2006).

[31] K.-E. Frøysa and P. Lunde, "Natural gas quality measurement using ultrasonic flow meters. development of a prototype gas analyzer with results from testing on north sea gas field data.", in *Proceedings of the 30th Scandinavian Symposium on Physial Acoustics, Geilo, Norway, 28-31 January 2007* (2007).

[32] H. Suzuki, H. Tanaka, and H. Hachisuka, "Method and apparatus for ultrasonic wave measurement", US Patent no. 6.094.987 (August 2000).

[33] ISO, "JCGM 100:2008: Evaluation of measurement data - Guide to the expression of uncertainty in measurement", International Organization for Standardization, Geneva, Switzerland (September 2008).

[34] E. Storheim, M. Aanes, M. Vestrheim, and P. Lunde, "Ultrasonic piezoceramic transducers for air, - finite element analysis and measurements", in *Proceedings of the 33rd Scandinavian Symposium on Physical Acoustics, Geilo, Norway, 7-10 February 2010*, edited by U. Kristiansen (2010).

Appendix A. Simulation parameters

Table A.1: Summary of some parameters used in the FEM simulations.

Parameter	Value
Radius of the piezoceramic disk	6.35 mm
Thickness of the piezoceramic disk	2.0 mm
Radius to infinite elements	2 cm
Meshing angle	1.3 radians
Meshing frequency	420 kHz
Start frequency	0 Hz
Step frequency	500 Hz
Stop frequency	400 kHz
Finite elements pr. shear wavelength (solids)	5
Finite elements pr. compressional wavelength (fluids)	5
Type of finite elements	8 node isoparametric
Material data for Pz27 and air	[34]